2013

Vertical structure of aerosols, temperature, and moisture associated with an intense African dust event observed over the eastern Caribbean

JOURNAL OF GEOPHYSICAL RESEARCH: ATMOSPHERES, VOL. 118, 4623–4643, doi:10.1002/jgrd.50352, 2013

Vertical structure of aerosols, temperature, and moisture associated with an intense African dust event observed over the eastern Caribbean

Eunsil Jung,[1] Bruce Albrecht,[1] Joseph M. Prospero,[1] Haflidi H. Jonsson,[2] and Sonia M. Kreidenweis[3]

Received 19 August 2012; revised 7 February 2013; accepted 15 March 2013; published 28 May 2013.

[1] An unusually intense African dust event affected a large area of the western Atlantic and eastern Caribbean in early April 2010. Measurements made east of Barbados from the Center for Interdisciplinary Remotely Piloted Aircraft Studies (CIRPAS) Twin Otter research aircraft are used to characterize particle size distributions; vertical distributions of aerosols, temperature, and moisture; and processes leading to the observed stratification in the boundary layer. The vertical profiles of various aerosol characterizations were similar on both days and show three layers with distinct aerosol and thermodynamic characteristics: the Saharan Air Layer (SAL; ~2.2 km ± 500 m), a subcloud layer (SCL; surface to ~500 m), and an intermediate layer extending between them. The SAL and SCL display well-mixed aerosol and thermodynamic characteristics; but the most significant horizontal and vertical variations in aerosols and thermodynamics occur in the intermediate layer. The aerosol variability observed in the intermediate layer is likely associated with modification by shallow cumulus convection occurring sometime in the prior history of the air mass as it is advected across the Atlantic. A comparison of the thermodynamic structure observed in the event from its origin over Africa with that when it reached Barbados indicates that the lower part of the SAL was moistened by surface fluxes as the air mass was advected across the Atlantic. Mixing diagrams using aerosol concentrations and water vapor mixing ratios as conserved parameters provide insight into the vertical transports and mixing processes that may explain the observed aerosol and thermodynamic variability in each layer.

Citation: Jung, E., B. Albrecht, J. M. Prospero, H. H. Jonsson, and S. M. Kreidenweis (2013), Vertical structure of aerosols, temperature, and moisture associated with an intense African dust event observed over the eastern Caribbean, *J. Geophys. Res. Atmos.*, *118*, 4623–4643, doi:10.1002/jgrd.50352.

1. Introduction

[2] It is common to observe the westward movement of dust-laden air from Africa over the tropical Atlantic Ocean under the influence of the trade winds [*Carlson and Prospero*, 1972]. The Saharan Air Layer (SAL) leaving Africa is formed by intense heating over the land and is thus characterized by a well-mixed layer that is warm (potential temperature of ~313 K–317 K) and dry (mixing ratios of ~2–4 g kg^{-1}), and extending from the surface to about 500 hPa over Africa, for example, during the summer [*Carlson and* Prospero, 1972; *Prospero and Nees*, 1977]. As the SAL moves off the coast of Africa, typically following an easterly wave, the base of the SAL is observed at higher levels (e.g., ~850 hPa in summer) as cooler and moister maritime air occupies the lower boundary layer [*Carlson and Prospero*, 1972; *Karyampudi and Carlson*, 1988; *Westphal et al.*, 1988; *Karyampudi et al.*, 1999; *Dunion and Velden*, 2004; *Nalli et al.*, 2005, 2006; *Wong and Dessler*, 2005; *Wong et al.*, 2006]. Individual SAL outbreaks can cover an area of the Atlantic as large as the 48 contiguous United States and can migrate to the eastern coast of Florida [*Dunion and Velden*, 2004]. The axis of the maximum dust concentrations shifts northward from ~5°N in winter to ~20°N in summer [*Moulin et al.*, 1997] due to the seasonal shift of the large-scale circulation patterns over Africa and the tropical Atlantic.

[3] The large amount of dust in the SAL substantially impacts the radiative balance of the earth-atmosphere system directly through scattering and absorption (e.g., reduced sea surface temperature; *Lau and Kim* [2007]) and indirectly by modifying cloud microphysics acting as effective ice nuclei [e.g., *DeMott et al.*, 2003; *Sassen et al.*, 2003] as well as cloud condensation nuclei in liquid clouds [e.g., *Twohy et al.*, 2009]. On other hand, the dry, dusty SAL may weaken

[1]Rosenstiel School of Marine and Atmospheric Science, University of Miami, Miami, Florida, USA.
[2]Center for Interdisciplinary Remotely-Piloted Aircraft Studies, Naval Postgraduate School, Monterey, California, USA.
[3]Department of Atmospheric Science, Colorado State University, Fort Collins, Colorado, USA.

Corresponding author: E. Jung, University of Miami, RSMAS/MPO, 4600 Rickenbacker Causeway, Miami, FL, USA. (eunsil.jung@gmail.com)

2169-897X/13/10.1002/jgrd.50352

the strength of tropical cyclones [*Dunion and Velden*, 2004; *Evan et al*., 2006; *Wu*, 2007] and suppress convection in the interior of the SAL [*Wong and Dessler*, 2005]. Further, the vertical structure of the absorbing aerosol layer (e.g., dust) can be important to aerosol-cloud-precipitation interactions since clouds can be suppressed or enhanced depending on the relative location of the absorbing aerosol layer [*Hansen et al*., 1997; *Feingold et al*., 2005; *Johnson et al*., 2004] and may also affect the profiles of atmospheric radiative forcing [e.g., *Ackerman and Chung*, 1992].

[4] The appearance of the multilayering of dust in the SAL has been reported since the early 1970s [*Prospero and Carlson*, 1972; *Karyampudi et al*., 1999; *Reid et al*., 2002; *Reid et al*., 2003]. However, studies of the mechanisms for the formation of the multilayering of dust are scarce; *Karyampudi et al*. [1999] suggested that dust in the lowest part of the boundary layer (subcloud layer in this study) was a residual of the initial SAL. On the other hand, *Reid et al*. [2003] argued that heavy dust in the boundary layer observed during the Puerto Rico Dust Experiment (PRIDE; July 2000) is transported across the Atlantic Ocean with its vertical character already defined as it leaves Africa.

[5] Although the general features of dust outbreaks over the ocean are known, questions remain regarding the vertical transport and processing of the dust and the details of the vertical structures of dust layers and the characteristics of each layer. Satellite-based studies can be used to study aerosol effects over a large geographical area for long time periods but are known to suffer from retrieval biases [*Loeb and Schuster*, 2008], and the vertical distribution, a key component of the aerosol indirect effect, is usually unknown. Lidar observations provide an excellent tool for illustrating the vertical distribution of aerosols. However, both ground-based and space-borne lidar observations are not always able to define the fine vertical structure of dust plumes when clouds are present [*Welton et al*., 2000; *Liu et al*., 2009; *Omar et al*., 2009].

[6] To observe cloud-aerosol interactions, associated with precipitating and nonprecipitating cumuli over the eastern Caribbean, the Barbados Aerosol Cloud Experiment (BACEX) was performed from 15 March to 15 April 2010. Operations were centered in a domain located over the ocean to the east and northeast of Ragged Point on Barbados (13.2°N, 59.5°W) as shown in Figure 1.

[7] The principal observing platform for the experiment was the Center for Interdisciplinary Remotely Piloted Aircraft Studies (CIRPAS) Twin Otter (TO) research aircraft that was equipped with aerosol, cloud, precipitation probes, and standard meteorological instruments. The vertical and horizontal distributions of aerosols observed on the 15 flights from the TO indicate a wide range of aerosol conditions that include the most intense African dust event observed at the Barbados Ragged Point surface site during all of 2010. In this study, we focus on two days of this dust event (1–2 April), when clouds were significantly suppressed. We combine the in situ aircraft data, which were obtained in an area just upstream from the Barbados Ragged Point surface site, with soundings at Barbados and western Africa to study the lower tropospheric thermodynamics at the source (Africa) and the local (Barbados) observational site and to define the vertical structures of aerosols and thermodynamics over the eastern Caribbean. Data used in this study are summarized in section 2. General information on flight patterns and profiles of thermodynamics and various aerosols are described in section 3, along with surface aerosol observations from Barbados and observations from a micropulse lidar (MPL) deployed at Ragged Point. Transports and processes affecting the observed aerosol structures are described in section 4. This section includes descriptions of mixing diagrams, particle size distributions, and hygroscopicity parameter kappa (κ). The summary and conclusions are given in section 5.

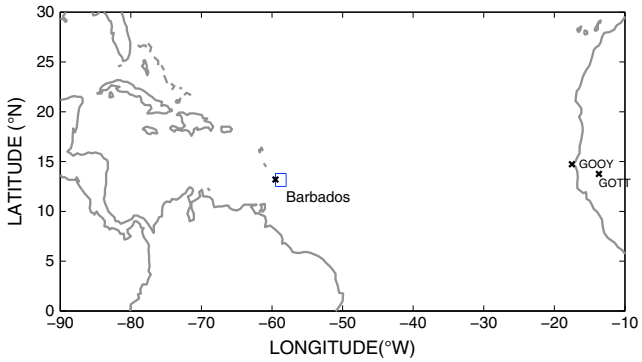

Figure 1. Location of data collection. Flight domain is shown as a square. Location of Barbados and two sounding stations over Africa, GOOY (Dakar, Senegal) and GOTT (Tambacounda, Senegal), are shown as cross symbols.

2. Data and Methods

2.1. Aircraft Data

[8] The CIRPAS Twin Otter research aircraft made 15 flights upstream from Ragged Point (13.2°N, 59.5°W), located on the eastern shore of Barbados where surface aerosol measurements were made (see section 2.2), from 19 March to 11 April. Each flight had durations of 3–4 h and included several horizontal level legs flown from near the ocean surface to above the trade winds inversion, and at least one pseudo sounding made as the aircraft either ascended or descended. The aircraft was equipped with aerosol, cloud, and precipitation probes and standard meteorological instruments for observing the mean and turbulent thermodynamic and wind structure. The aerosol data included aerosol concentrations from a passive cavity aerosol spectrometer probe (PCASP), a cloud condensation nuclei (CCN, Droplet Measurement Technologies (DMT) Inc.) spectrometer, and condensation particle counters (CPCs). The PCASP gave aerosol size distributions in the range of 0.1–2.5 μm over 20 bins. The dual-chamber DMT CCN spectrometer was set to give CCN concentrations at 0.3% and 0.6% supersaturations. Condensation nuclei (CN) measurements were made with CPCs with small-size cutoffs at 3 nm, 10 nm, and 15 nm. Aerosol data (PCASP, CN, and CCN) were obtained at 1 Hz resolution. Acronyms used in this study are listed in Table A1.

2.2. Ragged Point Aerosol Measurements

[9] Aerosol measurements are made at a site located on the edge of a 30 m high bluff on the easternmost coast of Barbados. Because Barbados is the easternmost of the Windward Islands and because of the trade winds, there

are no proximate upwind aerosol nonoceanic sources that could impact our measurements. Daily aerosol samples are collected at the top of a 17 m high tower using a high-volume (nominal $1\,m^3\,min^{-1}$) filter sampling system. To minimize impacts from local sources, sampling is electronically controlled to sample winds that blow from over the open ocean (i.e., within the sector extending from 335° to 130°) at wind speeds greater than $1\,m\,s^{-1}$. Filters are changed daily and periodically returned to Miami where the soluble components are extracted with water [*Li-Jones et al*., 1998]. The extracts were analyzed for major soluble inorganic ions: Na^+ by flame atomic absorption, and Cl^-, NO_3^-, and SO_4^- by suppressed ion chromatography [*Savoie et al*., 1989]. Sea salt aerosol concentrations are calculated from the Na^+ concentration based on the weight ratio of sea salt to Na, 3.256. The filters are then placed in a furnace at 500°C for 14 h; the filter ash is weighed after subtracting the filter blank (the ash weight of an unexposed filter which has been processed in the same manner as a sample filter) and is ascribed to mineral dust [*Prospero and Lamb*, 2003; *Trapp et al*., 2010]. The standard error in the mineral aerosol concentration is about ±10% for concentrations greater than about $1\,\mu g\,m^{-3}$.

[10] The Ragged Point site also supports a NASA aerosol robotic network (AERONET; *Holben et al*., [1998]) sun photometer and a NASA micropulse lidar network (MPLNET; *Welton et al*., [2000]) micropulse lidar. The photometer measures aerosol optical depth (AOD) at eight wavelengths (340, 380, 440, 500, 675, 870, 1020, and 1640 nm) and the Angstrom parameter in the wavelength interval of 440–675 nm (http://aeronet.gsfc.nasa.gov/new_web/units.html). The Angstrom exponent (α) is given by equation (1) for measurements of optical depth $\tau_{\lambda 1}$ and $\tau_{\lambda 2}$ that are taken at two different wavelengths λ_1 and λ_2.

$$\alpha = -\log\left(\frac{\tau_{\lambda 1}}{\tau_{\lambda 2}}\right) / \log\left(\frac{\lambda_1}{\lambda_2}\right) \quad (1)$$

[11] The exponent is inversely related to the average size of particles: the larger the particles, the smaller the exponent. Thus, the Angstrom exponent is useful when assessing the particle size of atmospheric aerosol. For example, dust usually has large sizes and thus a very smaller Angstrom exponent. We used level 2.0 data that were cloud screened and quality assured. Vertical structures of aerosols and clouds at Ragged Point were obtained from a micropulse lidar (MPL) system (http://mplnet.gsfc.nasa.gov/cgi-bin/Mplnet/site_page_direct.cgi/allsite=Ragged_Point).

2.3. Sounding Data and Back Trajectories

[12] To characterize boundary layer (BL) structures of SAL outbreaks both at their source (Africa) and over regions thousands of kilometers downstream (e.g., Barbados), daily rawinsonde observations from Grantley Adams Airport in Barbados [13.06°N, 59.48°W, World Meteorological Organization (WMO) ID: 78954], and Daker, Senegal (shown as GOOY in the text: 14.73°N, 17.50°W, WMO ID: 61641) and Tambacounda, Senegal (shown as GOTT: 13.76°N, 13.68°W, WMO ID: 61687) from western Africa are used. Sounding data were obtained from the University of Wyoming's online upper-air data (http://weather.uwyo.edu/upperair/sounding.html).

[13] The history of air mass sampled by the aircraft is estimated using the Hybrid Single Particle Lagrangian Integrated Trajectory (HYSPLIT) model from the average location (13.2°N, 59°W) of the flight domains (http://ready.arl.noaa.gov/HYSPLIT_traj.php). National Centers for Environmental Prediction (NCEP) reanalysis data using model vertical velocity for the vertical motion estimates are used as input meteorological gridded data for each flight. The 315 h backward trajectories, arriving at Barbados at 500 m, 1500 m, 3000 m, and 5000 m, are calculated to give a general sense of the origin of the air masses sampled on the aircraft missions.

3. Results

3.1. Between Source (Africa) and Site (Barbados)

[14] Dust concentrations recorded at the Barbados Ragged Point surface site during 2010 are shown in Figure 2. Dust and sea salt surface concentrations over the period of BACEX flights (19 March–11 April) are shown in the lower panel, along with AERONET level 2 aerosol optical depth (AOD) at 550 nm wavelength and Angstrom exponent at wavelength 440–675 nm.

[15] Dust concentrations during mid-March to mid-August in 2010 (Figure 2a) were often greater than $40\,\mu g\,m^{-3}$, which are considered to be major outbreaks of Saharan dust [*Prospero and Lamb*, 2003]. During the BACEX period (Figure 2b), Ragged Point dust concentrations remained lower than $10\,\mu g\,m^{-3}$ for a 9 day period, prior to 29 March, and then rapidly increased to a maximum on 1–2 April with concentrations higher than $150\,\mu g\,m^{-3}$ ($44.5\,\mu g\,m^{-3}$ on average, ranging from $0.7\,\mu g\,m^{-3}$ on 28 March to $155.1\,\mu g\,m^{-3}$ on 2 April). Throughout the BACEX period, sea salt surface concentrations ranged from $6.5\,\mu g\,m^{-3}$ on 4 April to $62.9\,\mu g\,m^{-3}$ on 10 April (on average, $20.2\,\mu g\,m^{-3}$). High and low surface sea salt concentrations correspond to the periods of weak (e.g., 3–4 April) and strong wind (e.g., $10\,m\,s^{-1}$ of low-level jet around 1 km on 10 April, shown in Figure 7a).

[16] Aerosol optical depth (AOD) fluctuates around 0.1 during the nondusty period then increases rapidly from 29 March. For 1 April, the AOD is observed to be about 0.6 at a wavelength of 500 nm. The peaks in AOD at around 25–26 March are associated with high concentrations of aerosol layers observed aloft during the period (not shown here). Angstrom exponents are less than 0.2 during the dust outbreaks and reach a minimum of 0.1 on 1 April, supporting the prevalence of dust during the period.

[17] The progression of the SAL outbreak across the North Atlantic including the BACEX period (19 March –11 April) suggests a series of SAL outbreaks, based on satellite imagery (available from UW-CIMSS tropical site archive: http://tropic.ssec.wisc.edu/archive/), analyses from the Navy Research Laboratory (NRL) Navy Aerosol Analysis and Prediction System (NAAPS) model (http://www.nrlmry.navy.mil/aerosol_web/index_frame.html), and soundings over Africa (http://weather.uwyo.edu/upperair/sounding.html). On 16 March, a large SAL event leaves the African coast and overspreads the North Atlantic for the next few days. Dust continues to stream off the Africa. On 22 March and 25–26 March, another surge of dust is apparent in the

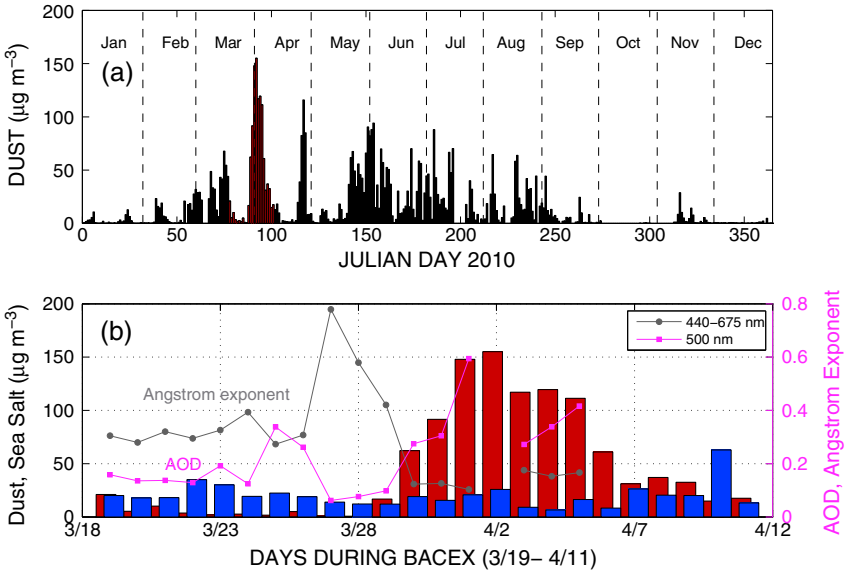

Figure 2. Dust concentrations recorded at the Barbados Ragged Point surface site (13.2°N, 59.5°W) during 2010. Dust surface concentrations (red) over the period of BACEX (19 March–11 April) are shown in the lower panel along with sea salt surface concentrations (blue) in the left axis, and level 2 aerosol optical depth (AOD) at 550 nm wavelength (magenta) and Angstrom exponent at wavelengths ranging from 440 to 675 nm (gray) from AERONET in the right axis. AOD and Angstrom exponent are not available on 2 April and between 6 April and 11 April 2010.

imagery and soundings over Africa. To get a general idea of when the air mass, which had a maximum surface concentration at the Barbados surface site on 1–2 April, left Africa and, thus, how long the SAL took to cross the Atlantic, 315 h (13 day) back trajectories arriving in Barbados at 17 UTC on 1–2 April were calculated (Figure 3). Ending points of 500 m, 1500 m, 3000 m, and 5000 m are examined. Overall, the back trajectories show that air mass, arriving at Barbados below 3 km, originated from Africa through easterly flow. On the other hand, the air mass arriving at Barbados above 3 km came from an area west of Barbados through westerly flow. Further, back trajectories, based on air mass arriving in Barbados at 500 m on 17 UTC 1 April 2010 (2 April 2010), for example, indicate that the air mass moved off the African coast on 22 March (26 March), indicating a 10 day (7 day) transit cross the Atlantic Ocean.

[18] NASA Moderate Resolution Imaging Spectroradiometer (MODIS) satellite images during 19 March and 2 April (http://modis-atmos.gsfc.nasa.gov/IMAGES/index.html) show a large amount of dust over Africa around 22 March (e.g., Figure 4b) that moves to a longitude of ~40°W (westernmost, in Figure 4a) 7 days later and then arrives at Barbados at around 1 April (not shown). The daily progression shown by individual satellite image (not shown) is roughly consistent with the back trajectories shown in Figure 3 during the experiment period. Therefore, based on the satellite images and the back trajectories, we estimate the transit time of the dust event from Africa to the Barbados area for this event to be 7–10 days. The unusually long transit of this event [7–10 day transit compared with a typical 5–7 day transit during the summer; e.g., *Prospero and Carlson*, 1972] may relate to the large-scale circulation pattern.

[19] A massive dust area extending from Africa to the Atlantic Ocean is also apparent in the aerosol optical depth product (Figure 5). The MODIS Collection 5 aerosol optical depth [*Levy et al.*, 2007; *Remer et al.*, 2005] processed using the methods of [*Zhang and Reid*, 2006; *Shi et al.*, 2011; *Hyer et al.*, 2011], averaged to a resolution of 1 degree. The imagery is available from NRL at http://www.nrlmry.navy.mil/aerosol, and the gridded MODIS data product is available from NASA LANCE: http://lance.nasa.gov. Daily averaged MODIS AOD product (pixel resolution is 1°) on 1 April 2010 (Figure 5c) clearly shows that areas of AOD higher than 0.45 (yellow to purple) extend from Africa to Barbados. The flight domain near Barbados is shown as a

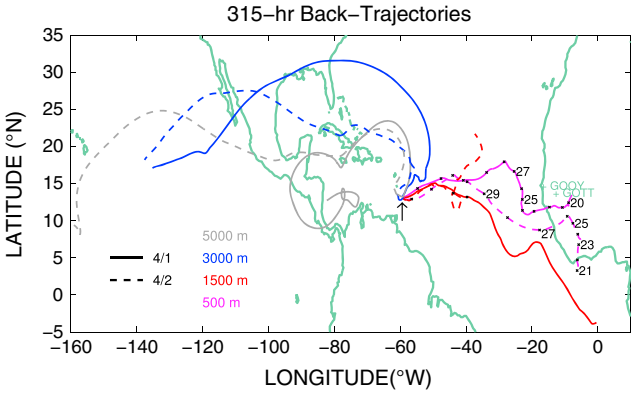

Figure 3. The 13 day back trajectory arriving at 500 m (magenta), 1500 m (red), 3000 m (blue), and 5000 m (gray) in the middle of the BACEX flight domain (shown as an end point of an arrow) for 17 UTC 1 April (solid) and 2 April (dashed) 2010. Trajectories of 500 m on each day at 00 UTC are denoted as cross symbols, and several dates of back-trajectory are shown accordingly. Locations of sounding stations at Africa used in Figure 6 are labeled.

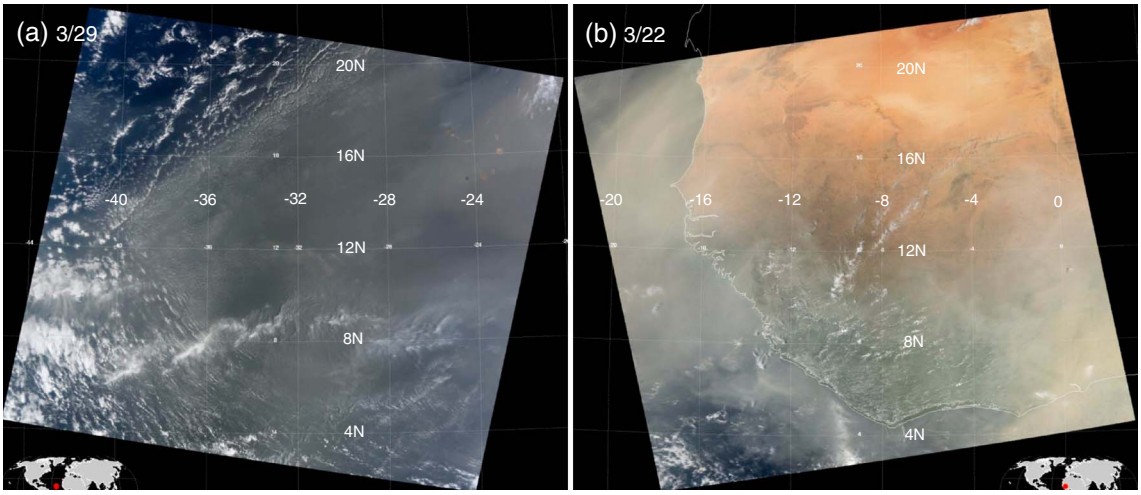

Figure 4. MODIS satellite images on (a) 29 March 2010 over the Atlantic and on (b) 22 March 2010 over western Africa. Images were downloaded from the MODIS website (http://modis-atmos.gsfc.nasa.gov/IMAGES/index.html).

square box and shows an AOD of 0.6–0.7, which is consistent with the AOD of 0.6 on 1 April measured from ground-based AERONET. It also shows that the area of high AOD (e.g., higher than 0.5, shown as orange) propagates westward during the experiment period. These dust dominant regimes look milky and turbid from MODIS satellite images in Figure 4. In addition, the clouds are significantly suppressed in the regimes of heavy dust, although low-level clouds are embedded in some areas of the dust.

[20] Profiles of potential temperature θ and mixing ratio r calculated from the Barbados rawinsondes on 1–2 April 2010 are shown in Figure 6, along with two soundings (Dakar and Tambacounda, Senegal) from western Africa (locations shown in Figure 1) on 21 and 22 March corresponding with the time period of the MODIS images shown in Figure 4. The air in and above the SAL observed at Barbados probably has not experienced significant moist processes. The satellite images during the 7–10 days of the transit across the Atlantic indicate no deep convection in the dust area, although some low-level clouds embedded in the dust are visible from satellite. Thus, in the SAL, one would expect that mixing ratio would be conserved.

[21] The SAL, shown as a well-mixed layer in θ and r, over Africa extends from 500 m to approximately 4000 m (depth of SAL: ~3500 m), but the top extends only to ~2650 m with a depth of ~800 m at Barbados after traveling over the Atlantic, suggesting the subsidence of SAL ~1250 m during the 10 days (~125 m d^{-1}). The potential temperature (in the SAL) at Africa (Figure 6a) is approximately 311–312 K but is about ~307 K at Barbados 10 days later, indicating a 4–5 K cooling over 7–10 days (a cooling rate of about 0.5°C d^{-1}). The moisture profile in the African SAL (Figure 6b) has a mixing ratio of ~4 g kg^{-1}, but a 5–6 g kg^{-1} mixing ratio is observed at Barbados. The differences in mixing ratio between Africa and Barbados may involve uncertainties about the locations and times of the SAL over Africa, and thus, we may see slightly different air masses within the SAL (as shown in section 3.3, Figure 9e). Regardless, we consider the mixing ratio difference of ~1–2 g

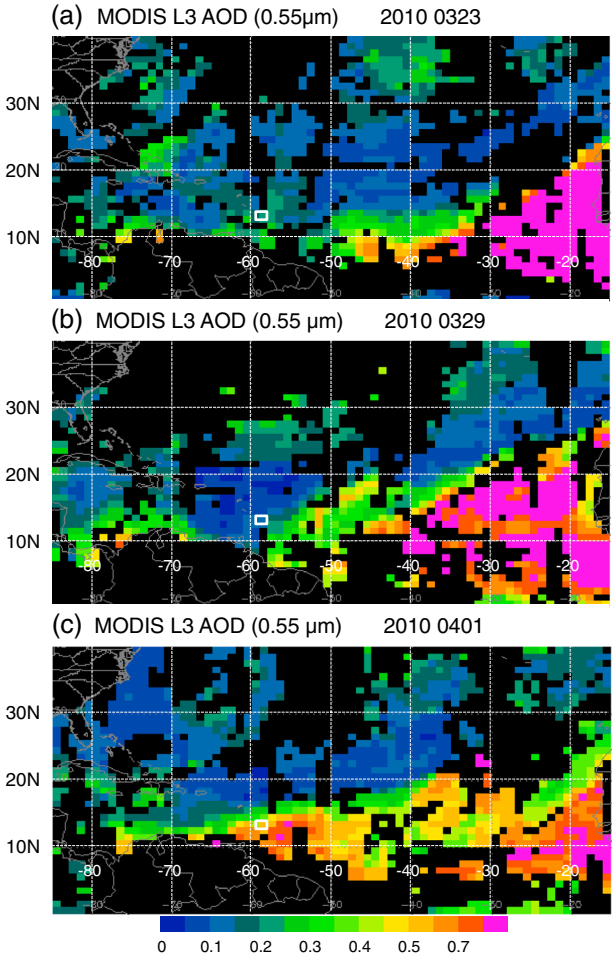

Figure 5. MODIS L3 aerosol optical depth at 550 nm wavelength. Images were downloaded from the NRL/Monterey Aerosol page (http://www.nrlmry.navy.mil/aerosol_web/index_frame.html). The flight domain is shown as a white-colored square symbol in the figure.

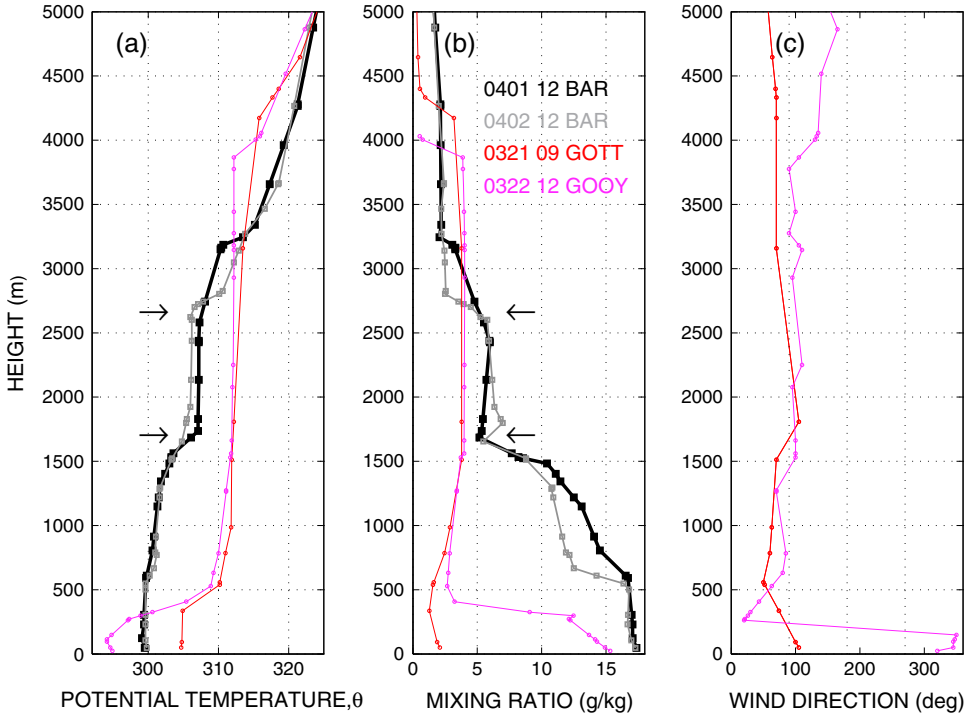

Figure 6. Profiles of (a) potential temperature and (b) mixing ratio on 21 March 09:00 UTC at GOTT (Tambacounda, Senegal) and 22 March 12:00 UTC at GOOY (Dakar, Senegal) in Africa, and on 1–2 April 12:00 UTC at Barbados. Profiles of wind direction on 21 March 09:00 UTC at GOTT and 22 March 12:00 UTC at GOOY in Africa are shown in Figure 6c. SAL observed at Barbados (approximate top and bottom) is denoted as arrows to give an idea of the location and depth of SAL over Barbados.

kg^{-1} in the SALs between Africa and Barbados to not be significant. The wind direction for the two African soundings (Figure 6c) indicates easterly winds throughout the layers, except for northerly winds close to the surface in the GOOY station that is close to the coast. As the SAL travels over the Atlantic, the boundary layer is modified by dry and moist convection; the difference between two groups of soundings (reddish from Africa and black/gray from Barbados) below the SAL (below ~1700 m, Figure 6), indicates the modification of boundary layer thermodynamics (and aerosols, as will be shown later) by cloud processes.

[22] We can estimate the fluxes needed to moisten the lowest layers of the deep mixed layer that originates over Africa. If we assume that the lower layers of the initial African soundings (0 to about 1700 m) are moistened by moisture fluxes from the surface and convective transports within the boundary layer, we can make a rough estimate of the average surface latent heat, along the trajectory using a simple moisture budget written as

$$\left.\frac{d\bar{r}_t}{dt}\right)_{\text{hor.}} = -\bar{w}\frac{\partial \bar{r}_t}{\partial z} - \frac{\partial}{\partial z}\left(\overline{w' r_t'}\right), \tag{2}$$

where $r_t = r + r_l$ is the total water mixing ratio, w is the vertical air velocity, and the overbar indicates a time/area average. On the left-hand side of this expression, we assume that the time rate of change of the liquid water mixing ratio can be neglected and that the total derivative is the horizontal component of the total derivative. The first term on the right side of the equation is the vertical advection term, which is a drying due to subsidence. The total water mixing ratio is used in the flux divergence term since moist convective transports (which include cloud transports of water) can alter the large-scale water vapor budget. If we consider a time average of equation (2) along the 10 day trajectory and a vertical average of the equation from the surface to the bottom of the SAL (Z_B; the height of the trade inversion), the budget equation can be written as

$$\frac{\overline{r_{BAR}} - \overline{r_{AFRICA}}}{\Delta t} = \overline{[Vert.Advection]} + \frac{\overline{w' r_0'}}{Z_B} \tag{3}$$

where it is assumed that the convective moisture flux at the base of the SAL is zero and the surface moisture flux is averaged over the 10 day trajectory. The left side of equation (3) is the estimated as the difference in the mixing ratio between the African and the Barbados soundings (Figure 6). Further, we assume that vertical velocity w is about $125\,m\,d^{-1}$ (top of SAL is about 3900 m over Africa on 22 March, and 2650 m at Barbados on 1 April) and the vertical gradient of mixing ratio is about 8 g $kg^{-1}\,km^{-1}$ from the difference of mixing ratio between the African and Barbados profiles for the lower marine boundary layer, e.g., $(18\,g\,kg^{-1} - 5\,g\,kg^{-1})/1700\,m$. With these estimates, the surface moisture flux needed to moisten the boundary layer along the 10 day transit from Africa to Barbados is estimated to be roughly $0.024 - 0.032\,g\,kg^{-1}\,m\,s^{-1}$, which corresponds to a latent hear flux ($\rho L_v \overline{w' q'}$) of ~60–80 Wm^{-2}. This surface latent heat flux estimated from the difference between the two soundings (Barbados and Africa), from the ocean surface to the bottom of the SAL (~1700 m in this case), is about the same as the

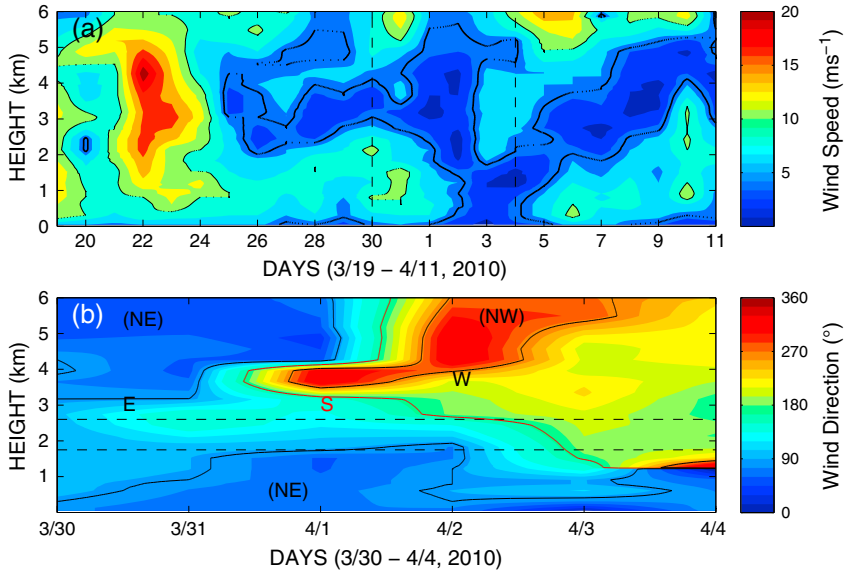

Figure 7. Time-height cross section of (a) wind speed (ms^{-1}) and (b) wind direction (degree) obtained from Barbados rawinsondes at 12 UTC (Figure 7a) during BACEX period (19 March–11 April 2010) and (Figure 7b) from 30 March to 4 April 2010 for period indicated by vertical dashed lines in Figure 7a. The approximate heights (bottom and top) of SAL, observed over Barbados (shown as arrows in Figure 6), are denoted as dashed lines in Figure 7b. Contours of wind speed of 5 m s^{-1} and 10 m s^{-1} (black-dotted) and wind directions of 90° (easterly, black), 180° (southerly, red), and 270° (westerly, black) are overlaid in Figures 7a and 7b, respectively.

climatological estimate for the surface annual moisture fluxes from the ocean surface (e.g., ~100 Wm^{-2} by *Wu et al*. [2007]). Thus, these budget estimates of the surface moisture flux imply that the modification of the boundary layer moisture structure can be explained by the dry and moist convective processes operating along the trajectory.

[23] Another possibility is that the air masses below the SAL (surface to ~1700 m) might have different source regions than the SAL (1700 m–2500 m) in Barbados and thus represent trajectories from very different areas. To investigate this possibility, the air mass extending from the surface to the top of the SAL that flows across the Atlantic was examined with NCEP reanalysis data. The reanalysis wind fields consistently show easterly flow at the surface, 900 hPa, 800 hPa, and 700 hPa, over the Atlantic, from Africa to Barbados (not shown here). This deep easterly flow is also consistent with the wind directions in the SAL shown in Figure 6c. Thus, the difference between two groups of soundings in the moist profile below SAL is not likely explained by differential advection. Further, the relative simplicity of the flow (deep easterly flow below 700 hPa) may help explain why the long-term trajectories with a 500 m ending point in Barbados (Figure 3) show good agreement with the observed advection of the dust mass across the Atlantic.

[24] Further, the possible changes in the local flow patterns over the period of this study, which may not be reflected by the large-scale NCEP reanalysis data described above, are examined using synoptic weather maps (not shown) and soundings obtained from the Barbados airport (Figure 7). A low with trailing cold front located SE of Cape Cod on 1 April 2010 moves south rapidly. By 12 UTC 2 April, the low is located near 32°N, 60°W, and the associated front is oriented roughly E–W across the northern Caribbean at ~17–18°N. As this front approaches the Caribbean, the low- to mid-level flow across the study region begins shifting from easterly to southwesterly. The time-height winds during this period from the Barbados soundings show this evolution (Figure 7). The time-height cross section of wind speed during the period of BACEX (19 March–11 April) is shown in Figure 7a, while the wind direction from 30 March to 4 April is shown in Figure 7b. The easterlies dominate throughout the atmosphere (up to 6 km) prior to 12 UTC 1 April. A layer of light (<5 m s^{-1}) and variable winds (S, SW, and NW) are found between 3 and 4 km on 1 April. On 2 April, the layer of southwesterly winds broadens and is observed right above SAL, but easterlies still persist in the low levels (surface to about 3 km; NE below SAL, SE within the SAL), which includes SAL over the Barbados. On 3 April, southwesterly flow descends from the top of the SAL to about 1500 m, indicating that the local flows have been changed after the dust event was studied. Analysis of dust and smoke from the NRL NAAPS model (http://www.nrlmry.navy.mil/aerosol_web/index_frame.html) for this period shows increasing concentrations of surface smoke with origins from South America. Nevertheless, Barbados is under the influence of easterlies from the surface to the top of the SAL. Therefore, we conclude that the SAL observed at Barbados during 1–2 April is not affected by smoke originating from South America, but it has been impacted by a single air mass (e.g., dust) with origins from Africa. However, there is a possibility that some smoke may have been present above the SAL on 2 April, but not within it.

3.2. Flight Paths

[25] On each of the two days studied, Twin Otter flights were made about 50–100 km upwind of Ragged Point and

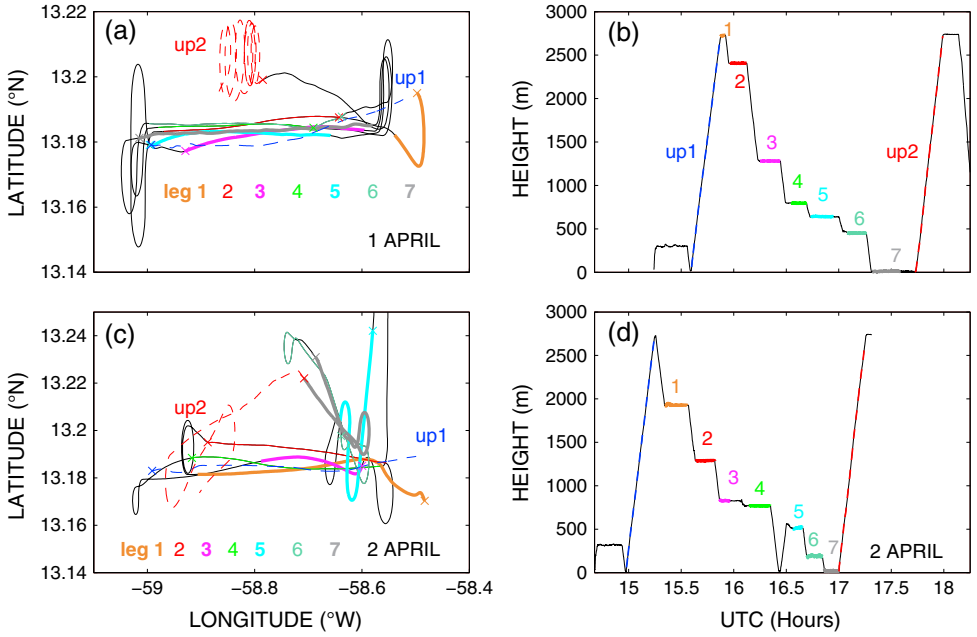

Figure 8. (a and c) Flight paths and (b and d) time series of flight altitudes on (Figures 8a and 8b) 1 April and (Figures 8c and 8d) 2 April 2010. Numerical numbers and colors are assigned to the individual level runs accordingly. Dashed lines in Figures 8a and 8c represent the first (up1) and second (up2) ascent soundings. Solid lines indicate data from level runs (leg 1 through leg 7). Legs 1, 3, 5, and 7 are denoted as bold lines in Figures 8a and 8c. The starting point of each leg is denoted as cross symbol in Figures 8a and 8c. The Barbados Ragged Point surface site is located at 13.2°N, 59.5°W.

included several constant-level legs (about 50 km in length) flown at heights from near the surface to about 3 km that were tied together by soundings made typically at the beginning and at the end of a sequence of level legs (Figures 8b and 8d). On 1 April 2010, no clouds were observed during the 3 h flight. The aircraft made seven level runs (Figures 8a and 8b), starting from the top of the SAL (labeled as leg 1 in Figure 8b) to ~30 m above the surface (leg 7) during a ~2 h period. The first sounding (labeled as up1 and shown in blue dashed lines in Figure 8) and level runs (leg 2 to leg 7) were made in the same upstream area from Ragged Point (Figure 8a). The second sounding (up2) was made slightly north (~2 km) of the first sounding. On 2 April 2010, two layers of heavy dust (with very heavy cirrus overcast advected from South America) were observed. There were very occasional cumulus clouds, generally in tiny patches and almost all very optically thin. Flight paths and time series of the altitudes flown on the day are shown in Figures 8c and 8d. The aircraft made seven level flights (called level runs, such as leg 1, leg 2, etc) on 1 April, but flight legs between 16:30 and 17:00 UTC (legs 5–7 during 16.5–17.0 h in Figure 8d) were made on the NE edge of the study area (see legs 5–7 in Figure 8c). However, the difference (~2 km and ~6 km to the north of the other level flights in Figures 8a and 8c, respectively) is negligible given a wind speed of 2–8 m s^{-1} (not shown here), with an advection distance of 8–30 km h^{-1}.

3.3. Thermodynamic and Aerosol Profiles

[26] Atmospheric thermodynamic (potential temperature and mixing ratio) profiles and aerosol concentrations from PCASP are shown in Figure 9 for the soundings obtained on the two flights. Observations from the level legs and the descents between these legs are also shown.

[27] The vertical profiles of potential temperature, water vapor mixing ratio, and aerosol concentrations obtained from PCASP (hereafter, simply PCASP) in Figure 9 indicate three layers with distinct aerosol and thermodynamic characteristics. The definition and illustration of the layers, used in this study, are based on the first sounding (up1) from 1 April shown in Figure 9a. A layer above the trade wind boundary layer (at about 1900 m to 2700 m) has well-mixed potential temperature, mixing ratio, and aerosol concentrations in the vertical and will be referred to as the Saharan Air Layer (SAL). A layer extending from the surface to about 500–600 m is well mixed and capped by a stable layer where mixing ratio decreases with height. This inversion (a narrow layer sits slightly above 500 m, referred to as the transition layer) is sufficiently strong to inhibit moist convection during most of the two flights (the strength of the transition layer is about 20 K km^{-1} on 1 April and 7 K km^{-1} on 2 April). However, for the traditional trade wind boundary layer [e.g., *Albrecht et al.*, 1979], a layer extending from the surface to about 500–600 m would be the subcloud layer (SCL). The third layer extending between the SAL and SCL will be referred to as the intermediate layer (IL) and displays the greatest temporal and spatial thermodynamic and aerosol variability. In terms of the classic trade wind boundary layer structure [e.g., *Augstein et al.*, 1974; *Albrecht et al.*, 1979], this IL would be called the cloud layer and is capped by the trade inversion. The variability in the thermodynamics and aerosol structure is illustrated by the difference between the first and second soundings. The second sounding was made about 2 h after the first one. A dry layer is found above the

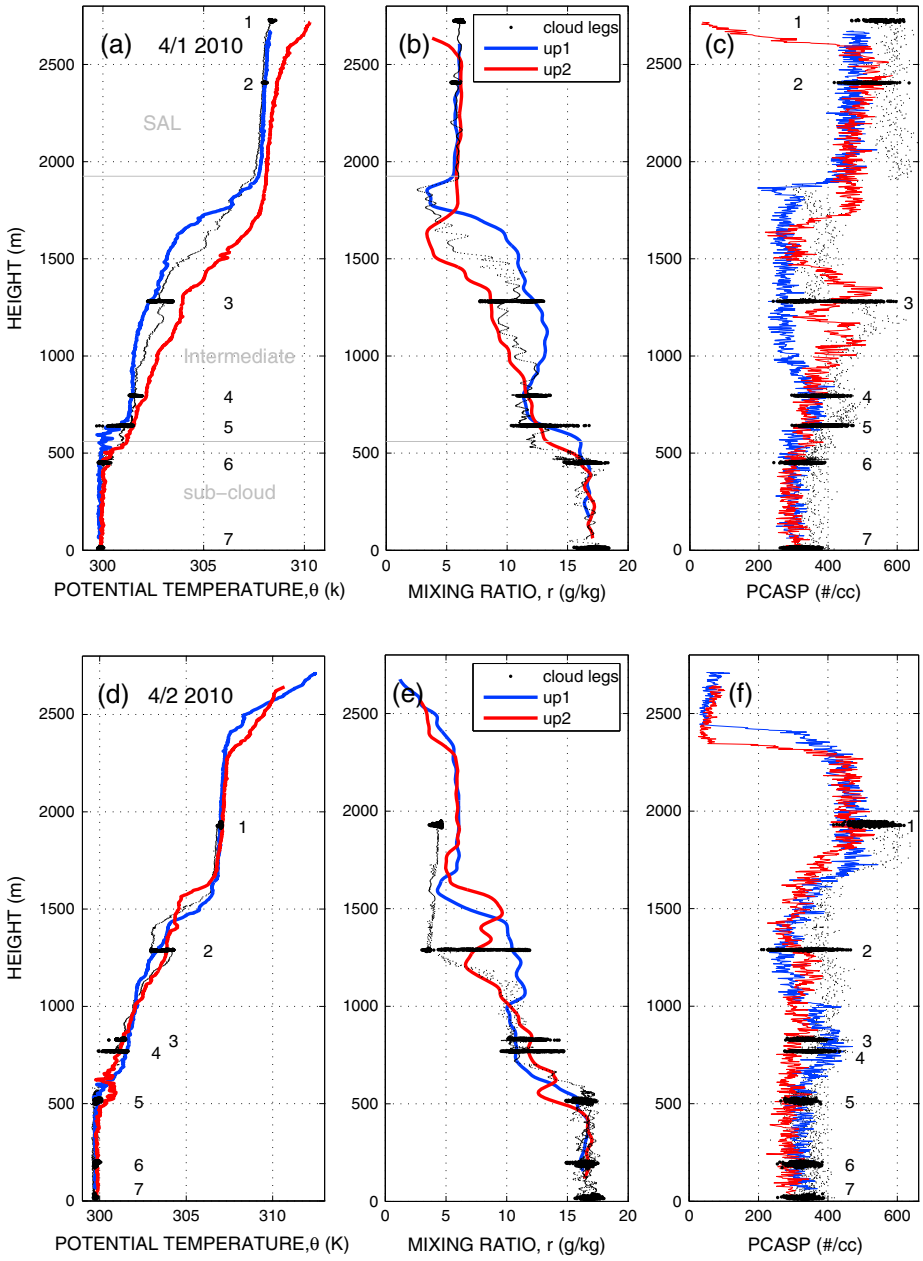

Figure 9. Profiles of (left) potential temperature θ, (middle) water vapor mixing ratio r, and (right) PCASP aerosol concentrations from aircraft during ascents. Data (10 Hz) from each level run are denoted by black bold colors and numbered accordingly. Thin black dots represent data obtained during descents between two consecutive legs. For 1 April 2010 (upper panel): leg 1, top of the haze layer; leg 2, middle of Saharan Air Layer (SAL); leg 3–leg 5, intermediate layer (IL); legs 6–7, subcloud layer (SCL). For 2 April 2010 (lower panel): leg 1, middle of Saharan Air Layer (SAL); legs 2–4, intermediate layer (IL); legs 5–7, subcloud layer (SCL). The layers of Saharan Air, intermediate, and subcloud are labeled in Figure 9a on the first sounding from 1 April to illustrate the layers.

SAL on both soundings on 2 April (above 2300–2400 m in Figure 9e) and in the second sounding on 1 April (above 2600 m in Figure 9b); but the first sounding on 1 April did not extend high enough to sample this layer.

[28] In Figures 9a–9c, the base of the SAL is about 200 m lower in the second soundings, and the largest aerosol variations occur in the IL. In addition, the second sounding on 1 April shows an intermediate layer (IL) that is warmer, drier, and dustier (this assumes that the aerosol in the intermediate layer are dust) than that observed on the first sounding.

[29] Although about 2 h of flight time separate the two soundings made on 2 April, the atmospheric thermodynamics and aerosols observed in the SAL and the subcloud layer show little change. However, alternating cool and warm (moist and dry) layers are observed throughout the intermediate layer. In Figure 9e, the cool and moist

layers are observed between 600 m and 1000 m, which were sampled on leg 3 and leg 4, and between 1450 m and 1700 m, which is close to the base of the SAL. Relatively lower concentrations of aerosols are observed in these cool and moist layers. These layers are most likely associated with modification by episodic shallow cumulus convection (through detrainment) sometime in the history of the air mass as it advected across the Atlantic. The intermittent nature of these convective events may explain the variability observed in the intermediate layer (IL) compared with that in the Saharan Air Layer (SAL) and in the subcloud layer (SCL). The horizontal variability within the IL, is also illustrated by the large variations found on the level legs (e.g., legs 3–5 for 1 April and legs 2–4 for 2 April) flown in this layer. The temperature and moisture in the SAL show little variability between soundings and little variability along the level legs flown in this layer.

[30] On 2 April (Figure 9e), a relatively dry layer is observed during leg 1 (shown as horizontal black dots; mixing ratio of ~4 g kg^{-1}) and during the descent between leg 1 and leg 2 (mixing ratio of ~6 g kg^{-1} from soundings). The mixing ratio of ~4 g kg^{-1} is consistent with that found in the SAL from the African soundings (GOTT and GOYY) in Figure 6. This feature [mixing ratios of ~6 g kg^{-1} and ~4 g kg^{-1} for the SAL, from soundings and level flights (e.g., leg 1) in Figure 9e] suggests that there is uncertainty in an air mass sampled at Barbados and that sampled from a fixed site in Africa as discussed earlier in section 3.1. The SAL may have a slight moisture variability in the horizontal (for example, ~1–2 g kg^{-1}), depending on the relative location from the center of the SAL. Air masses sampled between leg 1 and leg 2 show two distinctive thermodynamic characteristics (temperature and moisture), similar to that of either SAL or IL (not shown here).

3.4. Vertical Profiles of Various Aerosol Characterizations

[31] The vertical structure of the aerosols observed on the two flights show some complicated structures (Figure 9) but general features that are common to both days. To examine these structures in more detail, profiles of CN, CCNs, and PCASP were examined for the soundings made on 1–2 April 2010 (Figure 10).

[32] The layered structures are evident in the soundings made on both days (Note: aircraft soundings represent both vertical structure and horizontal variability). In the SAL, the concentrations of aerosols are greater than those of any of the other layers (Figures 10a–10d), and very low aerosol concentrations are found above the SAL (Figures 10b–10d). The SAL in the second sounding on 2 April (Figure 10d) is thinner with its top at about 2300 m, and its base is about 200 m higher (or slopes toward the south) than that in the first sounding in Figure 10c.

[33] Aerosol concentrations in the intermediate layer (IL) show the largest variability; for the first sounding on 1 April (Figure 10a), aerosol concentrations in the IL are slightly lower than those in the subcloud layer. However, the concentrations increased during the 2 h separation in the soundings and show aerosol concentrations that range between those of the SCL and those of the SAL in Figure 10b. For the first sounding on 2 April (Figure 10c), two layers with heavy aerosol are observed near leg 1 (middle of the SAL) and near the bottom of the IL. However, the layer of higher aerosol concentrations at the bottom of the IL is not present in the second sounding (Figure 10d); throughout the layer below leg 2 (surface to ~1250 m), aerosol concentrations show relatively well-mixed features but with a slight increase with height. In some parts of the intermediate layer (IL), the aerosol concentrations are lower than those in the subcloud layer (SCL), providing further evidence for possible cloud processing of the aerosols in the intermediate layer. Aerosol concentrations in the subcloud layer remain relatively constant (~200–400 cm^{-3}) during the course of the flights.

[34] The CCN (0.6%) and PCASP profiles are in good agreement throughout all the layers, but there are large differences between CCNs (at 0.3% and 0.6%; blue and red lines) as well as between CCN (0.3%) and PCASP (blue and black lines) below the heights of ~2400 m on both days. The largest differences are found near the center of the SAL, and the difference decreases closer to the surface. At the lower supersaturation (CCN 0.3% compared with CCN 0.6%), large particles are activated first. At the higher supersaturation (CCN 0.6% compared with CCN 0.3%), smaller particles can be activated too. Thus, the large difference between the two CCN profiles indicates the presence of small particles at those levels and/or that those particles are more hydrophobic.

[35] Although the potential temperature and mixing ratio are well mixed within the SAL (Figure 9), CCN (0.3%) concentrations increase rapidly with height above about 2400 m on both soundings on 1 April (Figures 10a and 10b) and approach the CCN (0.6%) and PCASP values near 2500 m. The collapses of the two CCN profiles and the PCASP profiles indicate that all the particles (small + big) at this level are activated even at the lower supersaturation measured, likely because particles at this level are more hydrophilic than in other levels. In addition, in the layer above the SAL on 2 April, the profiles have CCN concentrations that exceed those from PCASP, indicating the possible presence of small (less than 0.1 μm, the lowest resolvable size from the PCASP) CCN-active particles in this layer. These points will be further discussed in section 4.2.

3.5. MPL Aerosol Returns

[36] A further indication of the time (and implied spatial) evolution of the vertical structure of aerosols at the Ragged Point surface site, just downstream from the aircraft observations, is given by the lidar backscatter profiles. The normalized relative backscatters (so-called NRB signals, level 1 data), obtained from MPLNET on 1–2 April 2010, are shown in Figure 11. The MPL backscatter profiles for the 2 days include observations made during the aircraft flights, although the MPL is sheltered from the sun for a 1.5 h period around solar local noon (17 UTC).

[37] The backscatters from the subcloud layer (SCL), intermediate layer (IL), and Saharan Air Layer (SAL) show some of the same features shown by the vertical profiles from the aircraft observations. On 1 April, the top of the SAL increases from ~2 km to ~2.7 km from 00 to 14 UTC. The values of 0.33 (blue shading) and 0.67 (green shading) of normalized relative backscatters (NRB) are selected to define the top and bottom of the SAL, respectively. These threshold levels were subjectively selected after examining the height where there was a sudden decrease of aerosol extinction that occurred in the vertical profiles of aerosol

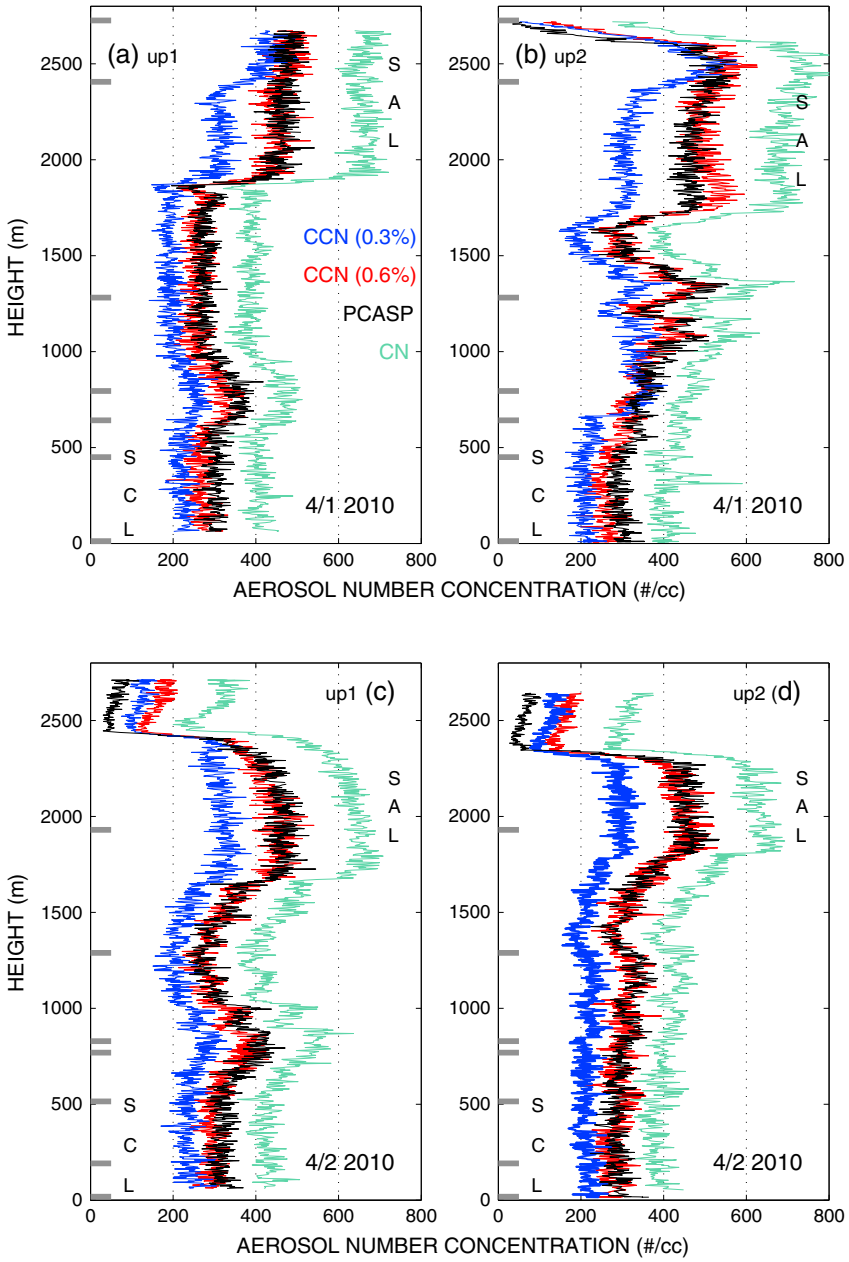

Figure 10. Profiles of various aerosols from various probes for (a, c) first (up1) and (b, d) second (up2) ascent soundings on (Figures 10a and 10b) 1 April and (Figures 10c and 10d) 2 April 2010. CN (green), PCASP (black), CCN (0.3%; blue), and CCN (0.6%; red) are shown. Average heights of individual level (~10 min) runs are denoted as thick gray horizontal lines (top down: leg 1 to leg 7). SAL and SCL are denoted. The layers between SAL and SCL indicate IL (intermediate layer). CCN (0.3%) indicates cloud condensation nuclei (CCN) activated at supersaturation of 0.3%. The same notation goes for CCN (0.6%). Information of data acquisition time and location is shown in Figure 8.

extinction. Some selected extinction profiles on 1 and 2 April 2010 are shown in Figure 11 as an example to show the heights of SAL top. From 18 UTC to about 12 UTC on 2 April, the top of the SAL fluctuates between 2.5 and 2.8 km (depicted as bluish colors). The top of the layer descends slowly after 12 UTC on 2 April, and a two-layered structure appears after 18 UTC. The separation of this upper layer is at a height of about 2.4 km. The descending features (of the top of the SAL and a layer above the SAL) are consistent with the temporal, and thus spatial, variability in the SAL shown by the soundings in Figure 9f.

[38] The lidar signal is attenuated backscattering. As a result, the signals decrease in strength with height even if the actual aerosol concentrations are higher aloft. Nevertheless, the NRB is useful to infer the interrelationship between clouds and aerosols by showing signals from both aerosols and clouds. In Figure 11, a multilayer structure is noticeable from 12 UTC on 1 April to the end of 2 April, especially

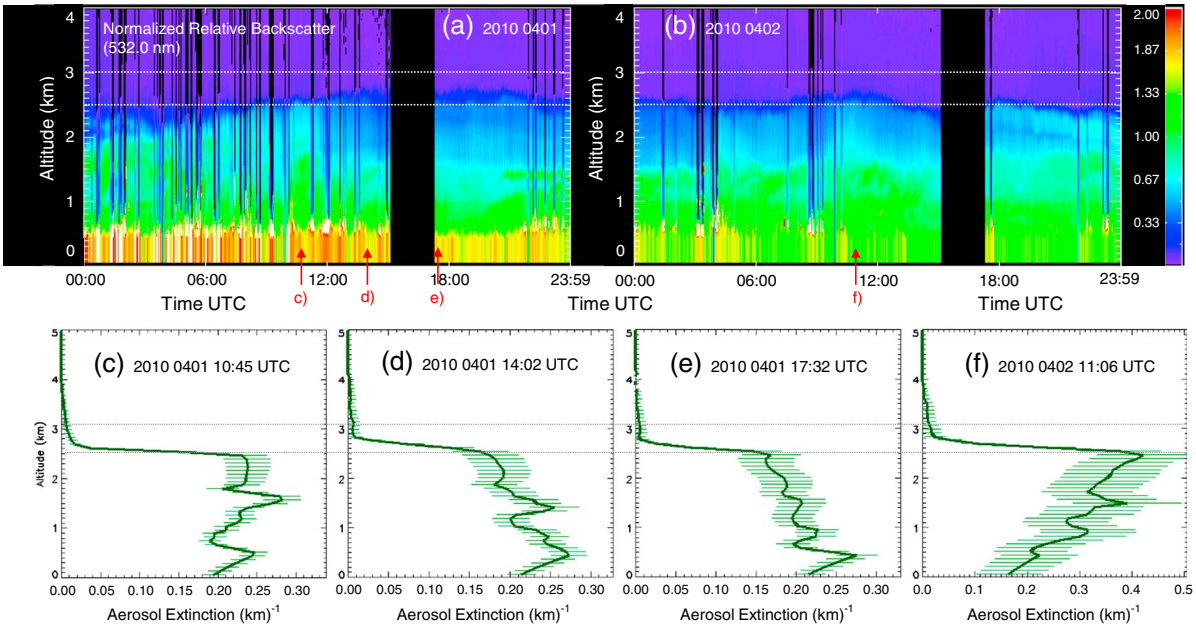

Figure 11. (Top; a and b) Time-height cross section of NRB (normalized relative backscatter) obtained from micropulse lidar (MPL) at Ragged Point in Barbados during 1–2 April 2010. The lidar is blocked from the sun for a 1.5 h period centered at around local noon and indicated by the dark areas in this figure. (Bottom; c–f) Some selected extinction profiles, denoted as upward pointing arrows in Figures 11a and 11b, on 1 and 2 April 2010 are shown to serve as a reference height for the SAL top. Horizontal lines denote the heights of 2.5 km and 3 km, respectively. Figures were obtained from MPLNET (http://mplnet.gsfc.nasa.gov/). Local time = UTC-5.

during the period of Twin Otter flights (15–18 UTC). The elevated high backscatter at ~500–1000 m (shown as white color) indicates clouds with bases near the bottom of the intermediate layer. These cloud returns are quite numerous prior to the flight on 1 April, but no clouds were observed during the flight. On 2 April, one strip of strong backscatter, an indicative of cloud, is seen near 1800 UTC. The lidar backscatter returns also show variability on scales that are consistent with the variability observed in the intermediate layer during the two flights.

4. Discussion of Transports and Processes

4.1. Mixing Diagram

[39] The possible processes affecting the nature of the observed aerosol layers are examined with mixing diagrams using conservative variables. A mixing diagram was originally used by *Paluch* [1979] to identify the source level of air entrained into the cloud using two conserved parameters that mix almost linearly. The source level of the entrained air into the cloud is defined as the height where the best-fit line through the in-cloud air property intersects the environmental curve. We adopted the concept of mixing diagram here. In this case, the water vapor mixing ratio and number concentration of aerosol per mass are assumed to be the conserved parameters and will mix almost linearly under dry condition. Mixing diagrams, formulated using mixing ratio and CCN (0.6%) per mass (Figure 12), are used to investigate the role of mixing processes on the aerosol distributions observed on 1–2 April 2010. The water vapor mixing ratio is plotted with decreasing values on the *y* axis, thus giving a rough sense of height.

[40] The mixing diagrams for both days show distinct clusters that are indicated by both level leg measurements and those from the profiles. For 1 April, the most significant variations in both moisture (mixing ratio) and aerosol concentration are observed in the upper and middle part of the intermediate layer. For example, leg 3 in Figure 12a shows two distinct populations of aerosol and moisture, suggesting strong horizontal variations at that level with two distinctive air masses—clusters of air masses with mixing ratios either higher or lower than 10 g kg^{-1}. Aerosols obtained at this level (leg 3) lie on a mixing line extending from the leg 1 (top of the SAL) and leg 2 (SAL) points (the best-fit line through the aerosol property at leg 3 intersects the environmental curve near leg 1 and leg 2 as well as aerosols at leg 1 and leg 2; the best-fit is not shown here). This mixing line is interpreted as aerosols observed on leg 3 sharing properties with aerosols observed on legs 1 and 2. Aerosols in leg 5 (lower IL), shown by magenta dots, connect to aerosols in leg 3 as well as those in leg 1 and leg 2, suggesting that aerosols in leg 5 were mixed with aerosols at those levels.

[41] The sounding shown in Figure 12 extends to the air at the top of the SAL and identifies a layer with dry air and low aerosol number concentrations (e.g., clusters with mixing ratio of ~4 g kg^{-1} and aerosol concentration of ~300 mg^{-1}). This air mass connects to mixing lines extending to the SAL (clusters with mixing ratios of about 6 g kg^{-1} and aerosol concentrations of 500 mg^{-1}, shown as blue dots), and the SAL air connects to the air mass in the intermediate layer as observed on leg 3 and leg 5.

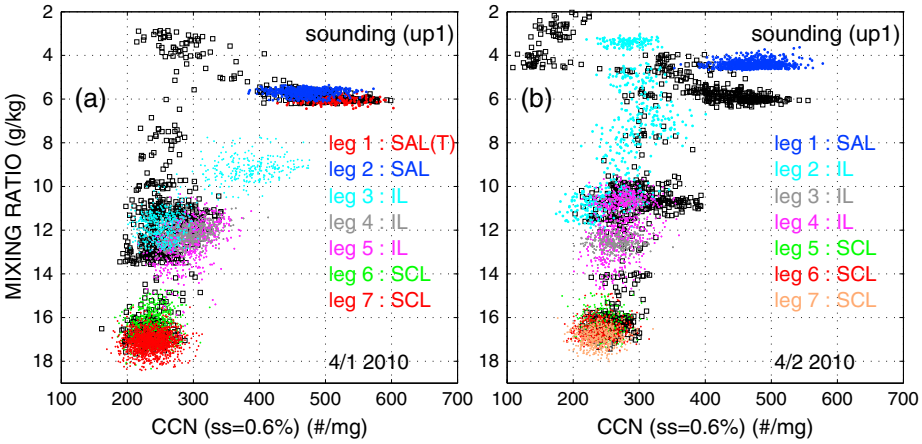

Figure 12. Mixing diagram of CCN (0.6%) per mass (mg^{-1}) and mixing ratio ($g\,kg^{-1}$) on (a) 1 April and (b) 2 April 2010. Black squares are obtained from the ascent environmental soundings, and colored dots are obtained from constant heights (level leg flight). (Figure 12a) Leg 1(top of the SAL; 2726 m), leg 2 (SAL; 2406 m), legs 3–5 (intermediate layer; 1281 m, 795 m, and 642 m), and legs 6–7 (subcloud layer; 450 m and 12 m); (Figure 12b) leg 1 (SAL; 1930 m), legs 2–4 (intermediate layer; 1289 m, 829 m, and 769 m), and legs 5–7 (subcloud layer; 514 m, 191 m, and 18 m).

[42] The SAL shows homogenous thermodynamic conditions, but varying CCN. For example, observations at leg 1 (top of the SAL) and leg 2 (SAL) on 1 April (Figure 12a) have similar moisture characteristics (mixing ratio of ~5–6 $g\,kg^{-1}$), while they show large variations in aerosol concentrations (400–600 mg^{-1} for CCN 0.6%). In contrast, the observations in the subcloud layer (for example, leg 7) have similar water vapor mixing ratios (~17 $g\,kg^{-1}$) and aerosol concentrations (~250 mg^{-1}) with a clustered distribution, rather than horizontally elongated pattern, as seen on legs 1 and 2. This pattern is more clearly seen in the mixing diagrams shown in Figure 13, where the variability within the various clusters is illustrated using CCN and CN observations.

[43] The mixing diagram for 2 April is shown in Figure 12b. The largest variability in the thermodynamic and aerosol characteristics is found on leg 2 in a layer below the SAL, which is similar to that on leg 3 of the 1 April case (Figure 12a). Aerosols sampled on leg 1 (SAL, blue dots) are associated with lower mixing ratios than those of the sounding sampled at the same height (e.g., clusters with mixing ratio of ~6 $g\,kg^{-1}$and CCN of ~400–500 mg^{-1}), indicating significant horizontal variations of aerosol at the same height and suggesting that aerosols in this region (leg 1, SAL) are associated with a drier air mass than that of the sounding shown in Figure 9e.

[44] Mixing diagrams for each level run for 1 and 2 April 2010 are shown in Figure 13. Aerosols in the SAL (Figures 13a, 13b, and 13f) show homogenous (well-mixed) thermodynamic conditions but varying CCN number concentrations, as indicated by the horizontally elongated pattern, while aerosols in the SCL (Figures 13e and 13i) show similar thermodynamics and aerosol characteristics, as indicated by the clustered pattern. Transports of aerosols from the SAL to the intermediate layer are seen in the upper to middle part of the intermediate layer in Figure 13c; and transports of aerosol within the intermediate layer, from the upper to lower parts of the layer, are seen in Figure 13g. Further, a connection between the aerosols in the lower part of the intermediate layer to those in the subcloud layer is seen in Figures 13d.

4.2. Size and Composition

[45] Aerosol particle size distributions (PSDs) from the PCASP differ among the layers and provide some insight into the processes operating on these various layers that affect the concentrations. The PSDs, in terms of $dN/d(\log D)$ and $dV/d(\log D)$, from the top of the SAL to the subcloud layer on 1 and 2 April 2010 are shown in Figure 14.

[46] The PSDs at all levels have a maximum concentration of particles in the range of $D < 0.5$ μm, with a maximum at 0.15 μm in the fine mode (Figures 14a and 14b), and show a secondary maximum at 0.8 μm for $D > 0.5$ μm representing the coarse mode. For 1 April, the largest population of small particles ($D <$ ~0.5 μm) is found near the top of the SAL (leg 1), although the larger particles ($D >$ ~0.5 μm) in this layer have smaller concentrations than those in the SAL and intermediate layers (legs 3–5 in Figure 14a). Among the intermediate layer profiles (legs 3–5), the upper part of the intermediate layer (leg 3) has more larger particles (especially larger than 1 μm) compared with the PSD in leg 5, which is closer to the bottom of the intermediate layer, indicating the presence of larger particles in the upper part of the intermediate layer (Figure 14a). Here, the upper part of the intermediate layer (leg 3) is drier than the lower part of IL (leg 5).

[47] Aerosol concentrations in the subcloud layer (legs 6–7 in Figure 14a) show consistently the lowest values during the flight, indicating that the main source of aerosols on this day is aloft, and not from the surface. Since similar results were found for the second case (2 April 2010), only a few distinct features are discussed here. One difference between the 1 April and 2 April cases is the presence of clouds on 2 April from samples taken near the bottom of the intermediate layer (legs 3–4), although the clouds are small and few in number. Since the aerosol probes (e.g., PCASP and CPCs) are known to have poor accuracy inside clouds, the aerosol data

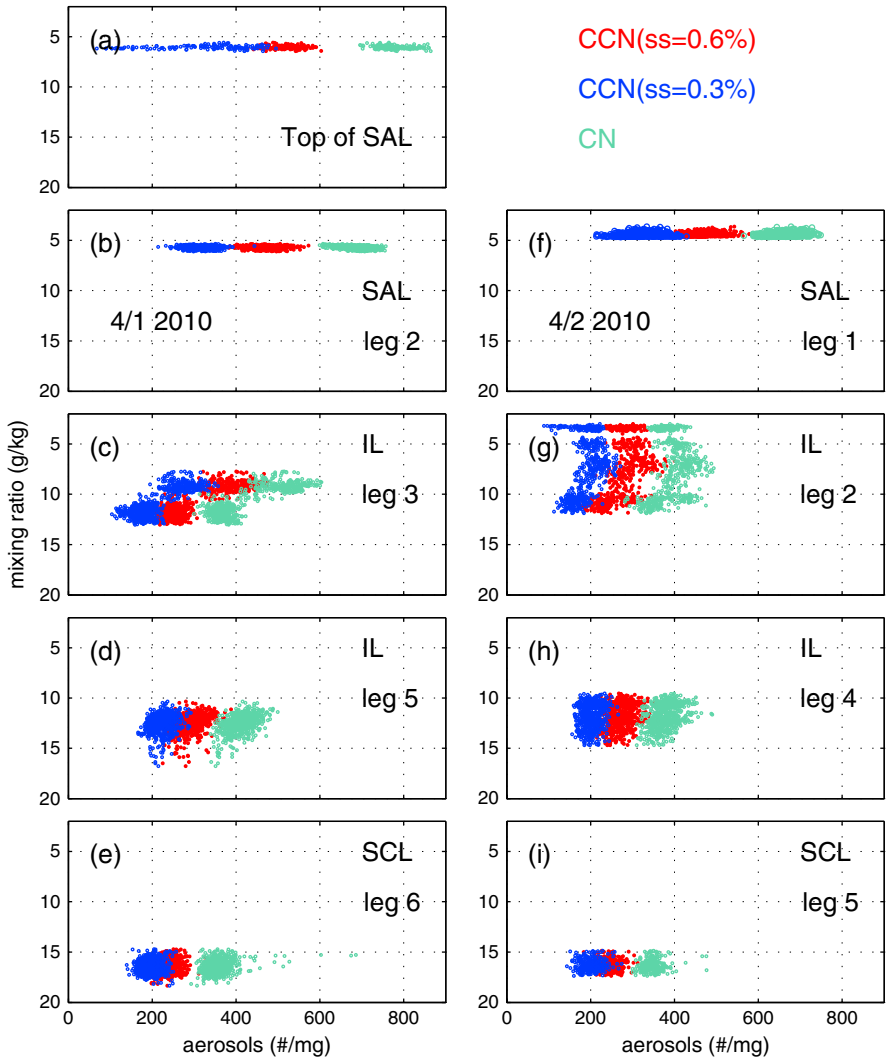

Figure 13. Mixing diagram of aerosol concentrations (mg^{-1}) for CCNs and CN versus mixing ratio ($g\,kg^{-1}$) for each level run for (a–e) 1 April and for (f–i) 2 April 2010.

obtained in-cloud were excluded from the analysis. On leg 1, in Figure 14b, the SAL has the most numerous particles over all ranges of sizes. In contrast, the subcloud layer has the lowest concentration of particles over all ranges, except at D ~0.2 µm. The upper part of the IL (leg 2 in Figure 14b) has the lowest concentrations of particles at D ~0.2 µm, and the second highest concentrations of large particles (especially $D > 0.5$ µm), suggesting the removal of fine particles and augmentation of coarse particles at this level. The mass of the particles is closely related to the particles' volume concentrations. In Figures 14a and 14b, although particle number concentrations are dominated by particles smaller than 0.5 µm in diameter, volume (mass) distributions are dominated by particles larger than 0.5 µm.

[48] To examine the effects of gravitational settling on changing the PSD, fall speeds were calculated. Particles with diameters of 0.15 µm and of 0.8 µm, which correspond to the two main peaks in PSDs, have fall velocities of approximately 5.8 cm d^{-1} and 1.6 m d^{-1}, respectively. Fall speeds of particles in the diameter range measured by the PCASP (0.1 µm–2.5 µm) lead to vertical displacements of 0.26 m to 160 m during 10 days of transport. Therefore, differential gravitational settling cannot explain the observed large variability in size distributions as a function of height.

[49] Profiles of mean (and standard deviations) of CCN (at 0.3% and 0.6%) number concentrations at each level are shown in Figure 15. To examine the contribution of small particles, the difference between CN and PCASP number concentrations, representing number concentrations for particles with diameters between approximately 3 nm and 0.1 µm, is also presented in Figure 15 at each level. This difference (CN – PCASP), shown as a black solid line, decreases from the SAL to the upper IL, increases slightly toward the bottom of the IL, and then increases sharply near the surface. The lowest number concentration of the small particles ($3\,nm < D < 0.1$ µm) is found in the intermediate layer [upper IL (~1250 m) on 1 April and the cloud layers (~800 m) on 2 April] and indicates some processing in this layer that removes the smaller particles, or lack of local source of small particles. The larger small-particle

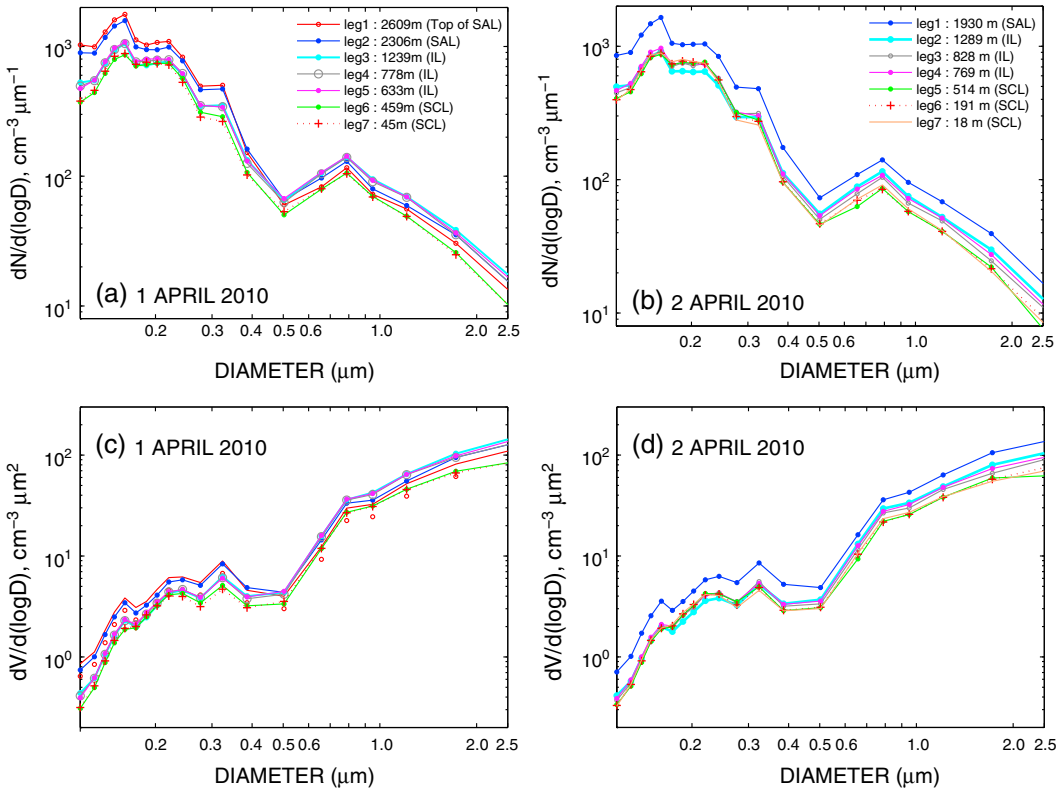

Figure 14. Aerosol particle size distributions for (a and c) 1 April 2010 from top of the SAL to subcloud layer and for (b and d) 2 April 2010 from SAL to subcloud layer. (Figures 14a and 14b) $dN/d(\log D)$; (Figures 14c and 14d) $dV/d(\log D)$.

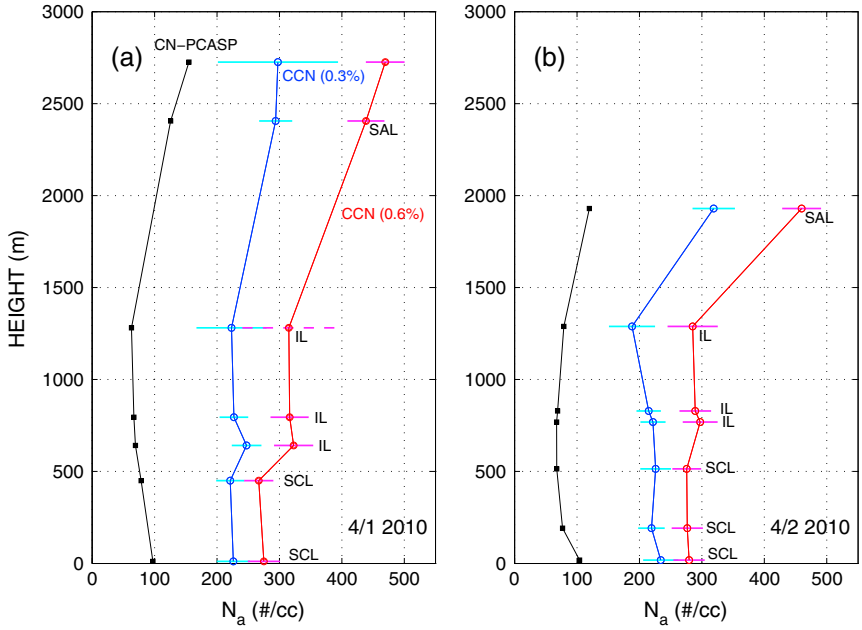

Figure 15. Mean profiles of CCNs (blue, CCN 0.3%; red, CCN 0.6%) at each level leg for (a) 1 April and (b) 2 April 2010. The difference of number concentrations between CN and PCASP at each level is also shown (black squares). Horizontal bar indicates $\pm 1\sigma$ from the mean value at each leg.

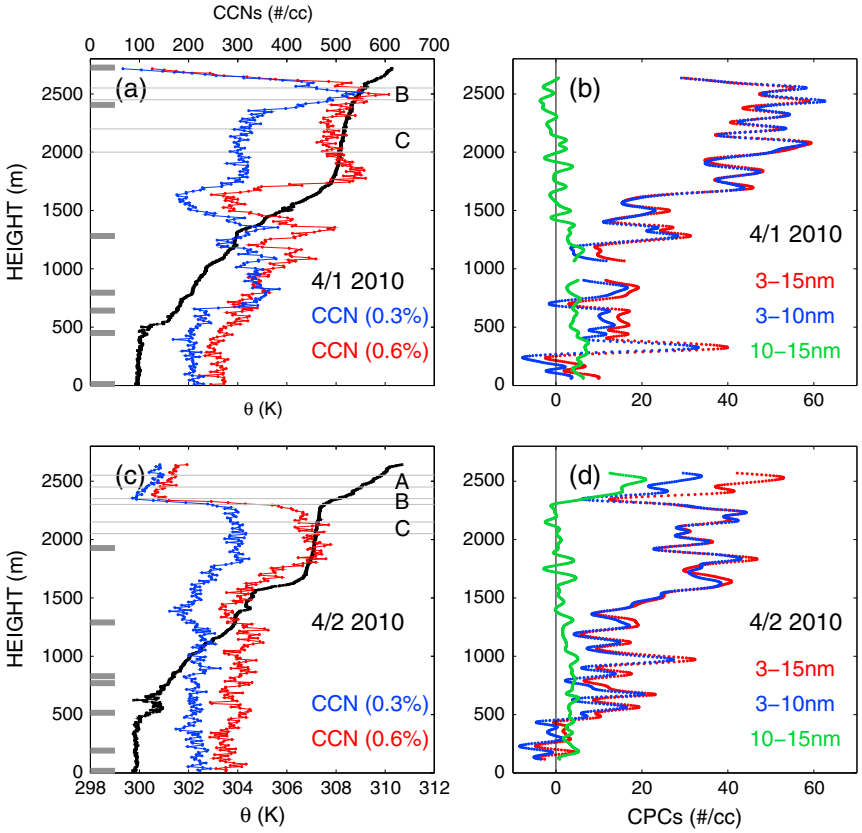

Figure 16. Profiles of (a and c) potential temperature (black solid line), CCNs (0.3%, blue; 0.6%, red), and (b and d) ultrafine aerosol concentrations (red, $3 < D < 15$ nm; blue, $3 < D < 10$ nm; green solid lines, $10 < D < 15$ nm) for the second soundings on (Figure 16a) 1 April 2010 and (Figure 16b) 2 April 2010. Average heights of individual level runs are denoted as thick gray horizontal lines (top down: leg 1 to leg 7) in Figures 16a and 16c.

concentrations in the subcloud layers indicate a possible source there, potentially due to the particles formed at the sea surface by bursting bubbles and consisting mostly of organic material [*de Leeuw et al.*, 2011]. As seen in Figure 10, differences between the CCN (0.3%) and CCN (0.6%) decrease closer to the surface, indicating a shift in the size distribution toward larger particles and/or the presence of more hydrophilic particles near the surface.

[50] Profiles of potential temperature and ultrafine aerosol concentrations for the second soundings on 1–2 April are

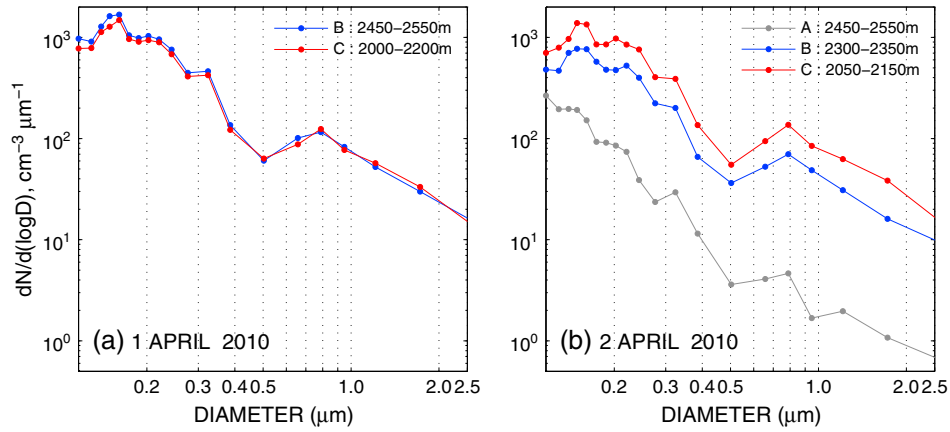

Figure 17. Aerosol particle size distributions calculated from the layers of A, B, and C in Figure 16, from the second soundings of (a) 1 April 2010 and (b) 2 April 2010. The layer A represents a layer above SAL, layer B indicates the very top of the SAL (Figure 17a) and a transit layer from the very top of the SAL to a layer above the SAL (Figure 17b), and layer C indicates the middle of the SAL. The locations of three layers are shown in Figure 16.

Table 1. The Critical Diameters (D_d) and Kappa (κ) at Each Level for 1–2 April 2010, With Values of k From Twomey [1959] and Number Concentration of CN – PCASP

1 April 2010						
Leg	Height		D_d (μm)	Kappa (κ)	CN – PCASP (# cm^{-3})	K from $N_c = Cs^k$
Leg 1	2726 m	Above SAL	0.18	0.025	155	0.78
Leg 2	2406 m	SAL	0.175	0.027	126	0.64
Leg 3	1281 m	IL	0.187	0.022	63	0.58
Leg 4	795 m	IL	0.185	0.023	67	0.57
Leg 5	642 m	IL	0.176	0.026	69	0.51
Leg 6	450 m	SCL	0.172	0.028	79	0.50
Leg 7	12 m	SCL	0.168	0.030	97	0.52
2 April 2010						
Leg	Height		D_d (μm)	Kappa (κ)	CN – PCASP	K from $N_c = Cs^k$
Leg 1	1930 m	SAL	N/A	N/A	121	0.58
Leg 2	1289 m	IL	0.182	0.024	79	0.66
Leg 3	829 m	IL	0.164	0.033	69	0.53
Leg 4	769 m	IL	0.165	0.032	67	0.52
Leg 5	514 m	SCL	0.167	0.031	68	0.46
Leg 6	191 m	SCL	0.172	0.028	77	0.50
Leg 7	18 m	SCL	0.164	0.033	104	0.50

shown in Figure 16. Ultrafine aerosol concentrations in three size ranges are obtained from the difference between lower detection limits of the CPCs: 3 nm $< D <$ 10 nm, 3 nm $D <$ 15 nm, and $10 < D <$ 15 nm. These differences were averaged five times over 12 s intervals to smooth out small-scale variability. Horizontal variations in the ultrafine number concentrations were observed on the level legs in the SAL (not shown) and may explain the variability observed in the profiles. Concentrations of aerosol particles with diameters between 3–10 nm and 3–15 nm are significantly higher in the SAL (~50 cm^{-3}) than in the other layers (e.g., less than 20 cm^{-3}). However, aerosol concentrations for particles with diameters between 10–15 nm are close to zero, indicating that the ultrafine particles are confined to the 3–10 nm size range. In contrast, the separations between the CPCs are evident in the clean layer above the SAL (e.g., Figure 16d), with 20 cm^{-3}of aerosol concentrations in the range $10 \text{ nm} < D < 15$ nm and 30 cm^{-3} in the range 3 nm $< D <$ 10 nm.

[51] In the SAL, newly formed extremely fine particles (3 nm $< D <$ 10 nm) may promptly coagulate with larger-sized particles, without creating particles in the 10–15 nm diameter range. However, in the layer above the SAL, where CCN and PCASP concentrations are very low, the rate of accumulation of the newly formed ultrafine particles onto larger particles will be inhibited. As a result, the small particles self-coagulate, and the resulting particles are observed in the 10–15 nm size range. The existence of extremely fine particles (3 nm $< D <$ 10 nm) in the SAL implies a source of aerosol in this layer.

[52] The number concentrations of CCN (0.3%) increase rapidly near the top of the SAL (a layer shown as B in Figure 16a) and lie on top of CCN (0.6%) as seen in Figure 10, thus indicating the presence of hygroscopic particles in the accumulation mode. In layer C (middle of the SAL), significant differences between CCN (0.3%) and CCN (0.6%) are found and imply one of two possibilities: first, if the composition is similar to that in the other layers, then a shift toward smaller particle sizes is anticipated; second, if particle size distributions are similar, then a shift toward less-hygroscopic particles relative to those in layers A and B is expected.

[53] To examine the differences in size distributions between layers, particle size distributions obtained from above the SAL (A—clean environment), at the very top of the SAL (B—a layer with similar CCNs), and in the middle of the SAL (C—a layer with large difference between CCNs) are shown in Figure 17. In Figure 17a, PSDs obtained from the top of the SAL (B) and those obtained from the middle of the SAL (C) on 1 April are almost identical in shape and concentration, indicating that the entire SAL is well mixed and thus has similar size distributions throughout, although layers B and C have substantially different CCN characteristics. Similarly, PSDs obtained from layers B and C on April 2 (Figure 17b) also show similar shapes in PSDs (bimodal shape with peaks at ~0.15 μm and ~0.8 μm), although layer B has lower aerosol concentrations in all size ranges. Considering both the particle size distributions and the CCN characteristics, more-hygroscopic particles are speculated to exist at the very top of the SAL (layer B). The PSD obtained from above the SAL (A, in Figure 17b) shows a distribution shape that is clearly different from that in the other layers. Overall, concentrations decrease with size and show no considerable peak either at ~0.15 μm or at ~0.8 μm, as shown from the other dust layers (e.g., layers B and C). Though, a slight peak at ~0.8 mm is shown from PSD obtained from above the SAL. The distribution indicates that particles sampled from above the SAL (layer A) have substantially different characteristics from those of the layers below (e.g., particles in the SAL, IL and, SCL).

[54] To infer the composition of aerosols at each level, first, critical dry diameters (D_d) for the CCN (0.3%) measurements were obtained by counting the particle numbers from the largest size, until the accumulated number equaled the number of CCN observed at that level (e.g., Figure 15). Then, for each level, the hygroscopicity parameter kappa (κ) was obtained by iteratively solving equation (6) in *Petters and Kreidenweis* [2007] for the κ that reproduces the setpoint supersaturation s_c of 0.3% for these critical diameters. The analytical approximation to this procedure that

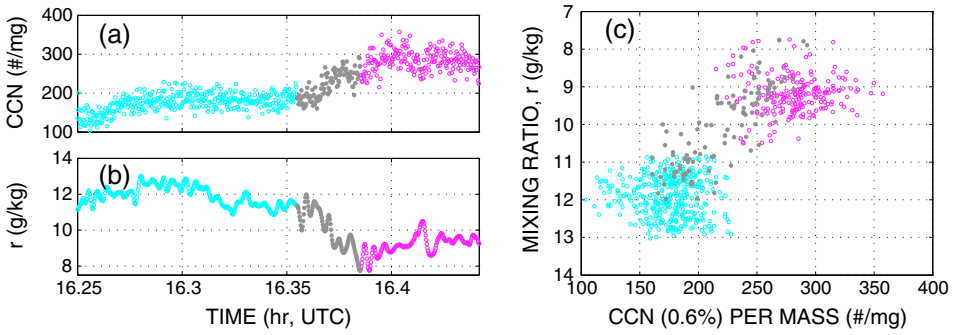

Figure 18. Time series of (a) aerosol number concentrations (CCN, 0.6% per mass) and (b) mixing ratio sampled on leg 3 (intermediate layer, IL) on 1 April for dry (magenta), moist (cyan), and transition (gray dots) ILs. A mixing diagram of aerosol concentrations (mg^{-1}) versus mixing ratio ($g\,kg^{-1}$) for these three air masses is shown in Figure 18c.

demonstrates the relationship between s_c, D_d, and κ more directly and is valid at $\kappa > 0.2$ is given by

$$\kappa = \frac{4A^3}{27D_d^3 \ln^2 s_c} \tag{4}$$

where the constant A is defined by

$$A = \frac{4\sigma_s/aM_w}{RT\rho_w} \tag{5}$$

where ρ_w is the density of water, M_w is the molecular weight of water, σ_s/a is the surface tension of the solution/air surface, R is the universal gas constant, and T is temperature. As discussed by *Petters and Kreidenweis* [2007], the parameter κ can be considered as a proxy for the aerosol chemical composition, with aerosols that are dominated by hygroscopic inorganic species having a κ of 0.5–1 and $\kappa = 0$ representing a nonhygroscopic but wettable aerosol. The procedure described above to obtain critical diameters and best-fit κ assumes that the entire aerosol size distribution, or at least that portion larger than the critical dry diameter, is internally mixed in composition and can be described by a single average κ. Critical dry diameters (D_d) and kappa (κ) for 1–2 April are summarized in Table 1 for the CCN (0.3%) measurements at each level. Number concentration differences between CN and PCASP (CN – PCASP), representing the number concentrations of ultrafine particles, are also shown in Table 1.

[55] For 1 April, the kappa values derived from the CCN (0.3%) measurement are fairly consistent throughout all the layers: a value of 0.026 on average (within a 10% standard deviation) and indicating the same species of aerosols (in this case, dust; kappa for pure dust = 0.01; *Petters and Kreidenweis* [2007]) at all levels. Note that hygroscopic particles at layer B in Figure 16 are not included in the level flight legs. The kappa values decrease slightly from the SAL to the upper/middle part of the IL and then increase closer to the surface, indicating that the particles are becoming more hydrophilic.

[56] For the 2 April observations, in general, kappa values have increased slightly compared with the previous day, possibly by aging or cloud processing (the addition of hygroscopic species via aqueous-phase processing). Kappa values are fairly consistent throughout all the layers, with a value of 0.02–0.03. However, kappa for leg 2 (upper part of the IL) has the smallest value, indicating that particles in this layer are least hygroscopic (note that no estimate is available for the SAL for the day). Further, kappa values are higher in legs 3 and 4, where clouds formed, possibly indicating cloud processing. The patterns of kappa are consistent with those of CN – PCASP in Figure 15.

[57] The CCN count can be approximated as $N_c = Cs^k$ [*Twomey*, 1959], where s is the percent supersaturation, and N_c and C correspond to CCN and CN in this study, respectively. The k values are also shown in Table 1. Overall, k values decrease closer to the surface and vary from 0.78 at the top of the SAL to 0.52 near the surface, indicating more continental aerosol characteristics in the air mass aloft when compared with particles near the surface (e.g., *Twomey* [1977]; k ~½ is typical for maritime environ-

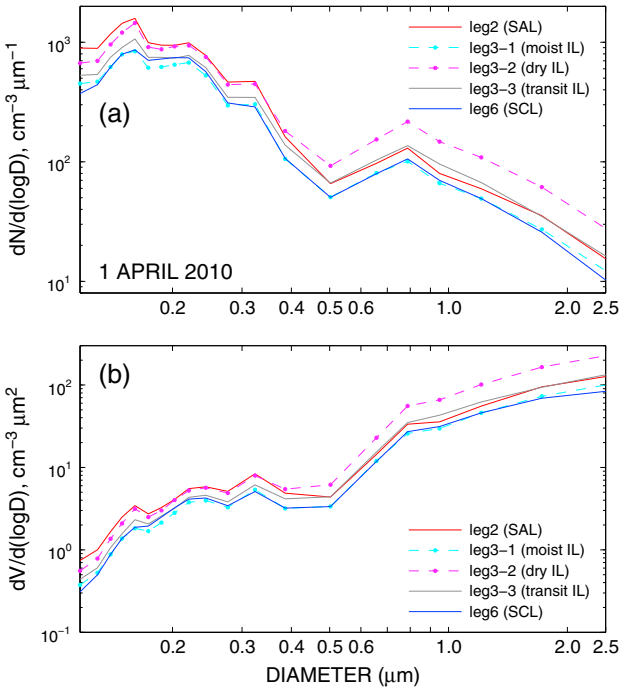

Figure 19. Aerosol particle size distributions (a) $dN/d(\log D)$ and (b) $dV/d(\log D)$ on 1 April 2010 obtained from the Saharan Air Layer (SAL), three intermediate layers (moist IL, dry IL, and transition IL), and the subcloud layer (SCL).

ment, and k ~2/3 is typical for continental air mass). In short, kappa and k indicate continental-type air masses in the SAL and maritime air masses from the surface to the lower IL, but with hygroscopicity associated with dust (kappa close to 0.01) throughout the BL.

4.3. Changes in Particle Size Distribution

[58] Two well-defined air mass populations are found in the intermediate layer (IL) on 1 April (e.g., Figures 12a and 18): a dry air mass with a water vapor mixing ratio of 9 g kg^{-1} and aerosol concentrations of 300 mg^{-1} (hereafter dry IL), and a moist air mass with a mixing ratio of 12 g kg^{-1} and aerosol concentrations of 200 mg^{-1} (hereafter moist IL). Air masses found between the moist and dry ILs will be referred to as the transition IL. To investigate the possibility of cloud processing on the changes in PSDs, aerosol distributions made on leg 3, associated with these three populations, are compared. The PCASP particle size distributions, in terms of $dN/d(\log D)$ and $dV/d(\log D)$, obtained from three intermediate layers (dry IL, moist IL, and transition IL), the Saharan Air Layer (SAL), and the subcloud layer (SCL) on 1 April, are shown in Figure 19.

[59] PSDs in the moist IL regime are similar to those in the subcloud layer over all ranges. PSDs in the transition IL regime look like a mixture of the SAL and the moist IL air masses; PSDs are close to those in the SAL in the range of $D > 0.5$ μm, and PSDs are close to those in the SCL for $D < 0.5$ μm. Particle size distributions obtained in the dry IL show similar characteristics to those in the SAL for the smaller particles ($D < 0.5$ μm) but have the highest concentrations of larger particles ($D > 0.5$ μm). The higher aerosol concentrations in the dry IL for $D > 0.5$ μm may indicate horizontal variations in the SAL; i.e., the drier, dustier parts of the SAL air masses are not sampled in the SAL leg (i.e., leg 2) but are sampled in the IL leg (leg 3-2 in Figure 19). Overall, the PSDs are shifted to lower concentrations in moister and cooler air masses. A comparison of PSDs from the moist IL with the PSDs from the dry IL suggests the removal of aerosol particles over all ranges by cloud processes, although precipitation processes occurring earlier in the history of the air mass may be involved too. As a layer is moistened (by comparing PSD changes from SAL to transition IL), number concentrations of smaller particles ($D < 0.5$ μm) decrease significantly, but larger particle concentrations ($D > 0.5$ μm) increase slightly (or change very little), suggesting coagulation processes occurring by the moistening process.

5. Summary and Conclusions

[60] Throughout the year, large amounts of dust from Africa are transported over the Atlantic to the Caribbean and westward with important implications for climate in these regions. The island of Barbados, located on the eastern edge of the Caribbean Sea, typically experiences northeast trade winds and periodic African dust outbreaks. In this study, an intense African dust event observed upstream (east) of Barbados on two days is studied using measurements from the CIRPAS Twin Otter research aircraft to characterize particle size distributions, condensation nuclei (CN), and cloud condensation nuclei (CCN). The vertical distributions of aerosols, temperature, and moisture are examined, and the processes leading to the observed stratification are considered.

[61] During the dust event studied, the surface observations from Ragged Point on Barbados indicate dust concentrations of about 155.1 μg m^{-3}, the highest concentrations observed for all of 2010, with an aerosol optical depth (at 550 nm) of about 0.6. The Saharan Air Layer (SAL) sampled during the flights was shown to have its origin over Africa 7–10 days prior to the observations. It originally had a potential temperature θ of ~312 K, a water vapor mixing ratio of ~4 g kg^{-1}, and a depth of ~3500 m over Africa. The SAL subsided about 125 m d^{-1} and was observed to have a depth of ~800 m at Barbados and a potential temperature θ of ~307 K, which is equivalent to a cooling rate of about 0.5°C d^{-1}.

[62] The observed vertical profiles of CCN, accumulation mode aerosol (PCASP), and CN concentrations indicate three layers with distinct aerosol and thermodynamic characteristics. These include the following: the SAL (Saharan Air Layer), IL (intermediate layer), and SCL (subcloud layer). The SAL and SCL are characterized as well-mixed layers, while the greatest thermodynamic and aerosol variability are observed in the IL. The highest aerosol concentrations were observed in the SAL, with CN and CCN ($s = 0.3\%$) concentrations of about 700 cm^{-3} and 300 cm^{-3}, respectively. Unexplained ultrafine (3–10 nm) particle concentrations of about 50 cm^{-3} were observed in the elevated SAL. The subcloud layer had CN and CCN concentrations of 400 cm^{-3} and 200 cm^{-3}. The intermediate layer had CN and CCN values between those observed in the SAL and SCL, as a whole.

[63] A comparison of the thermodynamic structure observed in the dust event over Africa with that at Barbados indicates that layers below the SAL (from surface to 1700 m) were moistened by surface fluxes (latent heat flux estimated to be about 60–80 W m^{-2}) as the air mass moved across the Atlantic over 7–10 days. The cool and moist layers in the IL corresponded to the lower concentrations of aerosols. These layers are most likely associated with modification by episodic shallow cumulus convection sometime in the previous history of the air mass as it advected across the Atlantic. The intermittent nature of these convective events explains the variability observed in the IL compared with that in the SAL and in the SCL. Further, in some parts of the intermediate layer, the aerosol concentrations are lower than those in the subcloud layer, providing further evidence for possible cloud processing of the aerosols in the intermediate layer. Time-height observations from the micropulse lidar (MPL) located at Ragged Point also indicate mesoscale variability in the IL aerosols.

[64] Mixing diagrams using aerosol concentrations and mixing ratios as conserved thermodynamic parameters provide insight into the vertical transports and mixing processes operating within the multilayered structure. Aerosols in the intermediate layer share their thermodynamic and aerosol characteristics with those in the SAL, suggesting that the aerosols in the IL in this study are derived from those in SAL. The estimated hygroscopicity parameter, kappa (κ, a proxy for chemical composition), ranged between 0.022 and 0.033. These low values, similar to those expected for dust, confirmed that dust was present in all layers during the event. Small hygroscopic particles that have the same particle size distribution as those in the SAL were observed at the very top of the SAL and were possibly dust coated with hydrophilic material.

[65] Changes in particle size distributions due to cloud processing were examined in three distinctive air masses that were sampled in intermediate layers: dry, moist, and transition ILs. This study showed that air masses in the moist IL have been processed by convection and, thus, have characteristics similar to those in the SCL, while the dry air masses have characteristics similar to those in the SAL. The transition air masses have characteristics similar to those of both the SAL and the SCL.

[66] This study has documented the vertical structure of aerosols associated with intense dust events and helps put into perspective the observations of dust concentrations and AOD, observed from surface measurements and satellite measurements from the top of the atmosphere. The SAL layer is often referred to as an elevated layer. The aerosol characteristics in the layers below SAL are similar to those in the SAL but with aerosol concentrations somewhat reduced. However, the thermodynamic structure below the SAL is substantially modified by dry and moist convective processes in the boundary layer. Further, the presence of dust in and above the boundary layer may impact the modification of the boundary layer by modulating convective and radiative processes as the air flows westward across the North Atlantic.

[67] The observations and analyses presented in this study may have the potential for evaluating simulations from models ranging from large-scale to cloud-resolving models. Several aerosol, cloud, and boundary layer processes need to be represented or parameterized in these models to adequately simulate the downstream evolution of the boundary layer structure. These processes include aerosol processing and transports associated with dry and moist convections, and direct and indirect aerosol effects that involve both radiative and convective processes. Adequate simulation of the boundary layer structure may be particularly important in affecting the environment of tropical cyclones, the evolution of tropical waves, and long-term climate realizations for the Atlantic. Further study is clearly needed to understand the evolution of the SAL as it is advected across the Atlantic, such as processes that affect aerosol and thermodynamic properties of the layer, and the thermodynamic and aerosol structure below the SAL.

Appendix A

Table A1. Table of Acronyms

Acronym	Expression
AOD	Aerosol optical depth
AERONET	Aerosol robotic network
BACEX	Barbados Aerosol Cloud Experiment
BL	Boundary layer
CCN	Cloud condensation nuclei
CIRPAS	Center for Interdisciplinary Remotely Piloted Aircraft Studies
CN	Condensation nuclei
CPC	Condensation particle counter
DMT	Droplet Measurement Technologies
HYSPLIT	Hybrid Single Particle Lagrangian Integrated Trajectory
IL	Intermediate layer[a]
MPLNET	Micro pulse lidar network
NRB	Normalized relative backscatter
PCASP	Passive cavity aerosol spectrometer probe (0.1–2.5 μm)
PSD	Particle size distribution
SAL	Saharan Air Layer
SCL	Subcloud layer[b]

[a]This layer is the same as a traditional convective boundary layer.

[b]This layer extends from surface to ~500–600 m.

[68] **Acknowledgments.** We thank all the individuals who assisted in making the observations from the CIRPAS Twin Otter during BACEX. A particular note of appreciation is due to Patrick Chuang of University of California Santa Cruz and David Painemal of the University of Miami, who were the onboard observers during the April 1 and April 2 flights. We are very appreciative of the comprehensive review and constructive comments provided by an anonymous reviewer. We thank Judd Welton and his staff for establishing and maintaining the Ragged Point MPLNET sites used in this investigation. Figure 11 is obtained from MPLNET (http://mplnet.gsfc.nasa.gov/). The authors gratefully acknowledge the NOAA Air Resources Laboratory (ARL) for the provision of the HYSPLIT transport and dispersion model and/or READY website (http://ready.arl.noaa.gov) used in this publication. Figure 4 is downloaded from the MODIS satellite website (http://modis-atmos.gsfc.nasa.gov/IMAGES/index.html). Images of MODIS AOD in Figure 5 were downloaded from the Naval Research Laboratory/Monterey Aerosol page (http://www.nrlmry.navy.mil/aerosol_web/index_frame.html). Sounding data in Figures 6 and 7 were obtained from the University of Wyoming's online Upper Air Data (http://weather.uwyo.edu/upperair/sounding.html). This study was funded by ONR grant N000140810465.

References

Ackerman, F. A., and H. Chung (1992), Radiative effects of airborne dust and regional energy budget at the top of the atmosphere, *J. Appl. Meteor.*, *31*, 223–233.

Albrecht, B. A., A. K. Betts, W. H. Schubert, and S. K. Cox (1979), A model of the thermodynamic structure of the trade-wind boundary layer. Part I: Theoretical formulation and sensitivity tests, *J. Atmos. Sci.*, *36*, 90–98.

Augstein, E., H. Schmidt, and F. Ostapoff (1974), The vertical structure of the atmospheric planetary boundary layer in undisturbed trade winds over the Atlantic Ocean, *Bound.-Layer Meteor.*, *6*, 129–150.

Carlson, T. N., and J. M. Prospero (1972), The large-scale movement of Saharan air outbreaks over the northern equatorial Atlantic, *J. Appl. Meteor.*, *11*, 283–297.

DeMott, P. J., K. Sassen, M. R. Poellot, D. Baumgardner, D. C. Rogers, S. Brooks, A. J. Prenni, and S. M. Kreidenweis (2003), African dust aerosols as atmospheric ice nuclei, *Geophys. Res. Lett.*, *30*, doi:10.1029/2003GL017410.

de Leeuw, G., E. L. Andreas, M. D. Anguelova, C. W. Fairall, E. R. Lewis, C. O'Dowd, M. Schulz, and S. E. Schwartz (2011), Production flux of sea spray aerosol, *Rev. Geophys.*, *49*, RG2001, doi:10.1029/2010RG000349.

Dunion, J. P., and C. S. Velden (2004), The impact of the Saharan air layer on Atlantic tropical cyclone activity, *Bull. Amer. Meteor. Soc.*, *85*, 353–365.

Evan, A. T., J. Dunion, J. A. Foley, A. K. Heidinger, C. S. Velden (2006), New evidence for a relationship between Atlantic tropical cyclone activity and African dust outbreaks, *Geophys. Res. Lett.*, *33*, L19813, doi:10.1029/2006GL026408.

Feingold, G., H. Jiang, and J. Y. Harrington (2005), On smoke suppression of clouds in Amazonia, *Geophys. Res. Lett.*, *32*, L02804, doi:10.1029/2004GL021369.

Hansen, J., M. Sato, and R. Ruedy (1997), Radiative forcing and climate response, *J. Geophys. Res.*, *102*, 6831 – 6864.

Holben, B. N., et al. (1998), AERONET – A federated instrument network and data archive for aerosol characterization, *Rem. Sens. Environ.*, *66*, 1–16.

Hyer, E. J., J. S. Reid, and J. Zhang (2011), An over-land aerosol optical depth data set for data assimilation by filtering, correction, and aggregation of modis collection 5 optical depth retrievals, *Atmos. Meas. Tech.*, *4*, 379–408, doi:10.5194/amt-4-379-2011.

Johnson, B. T., K. P. Shine, and P. M. Forster (2004), The semidirect aerosol effect: Impact of absorbing aerosols on marine stratocumulus, *Q. J. R. Meteor. Soc.*, *30*, 1407–1422.

Karyampudi, V. M., and T. N. Carlson (1988), Analysis and numerical simulations of the Saharan air layer and its effect on easterly wave disturbances, *J. Atmos. Sci.*, *45*, 3103–3136.

Karyampudi, V. M., et al. (1999), Validation of the Saharan dust plume conceptual model using lidar, Meteosat, and ECMWF data, *Bull. Amer. Meteor. Soc.*, *80*, 1045–1075.

Lau, K. M., and K. M. Kim (2007), Cooling of the Atlantic by Saharan dust, *Geophys. Res. Lett.*, *34*, L23811, doi:10.1029/2007GL031538.

Levy, R. C., L. A. Remer, S. Mattoo, E. F. Vermote, and Y. J. Kaufman (2007), Second-generation operational algorithm: Retrieval of aerosol properties over land from inversion of moderate resolution imaging spectroradiometer spectral reflectance, *J. Geophys. Res.-Atmos.*, *112*, D13211, doi:10.1029/2006JD007811.

Li-Jones, X., H. B. Maring, and J. M. Prospero (1998), Effect of relative humidity on light scattering by mineral dust aerosol as measured in the

marine boundary layer over the tropical Atlantic Ocean, *J. Geophys. Res.*, *103*(D23), 31,113–31,121, doi:10.1029/98JD01800.

Liu, Z., M. Vaughan, D. Winker, C. Kittaka, B. Getzewich, R. Kuehn, A. Omar, K. Powell, C. Trepte, and C. Hostetler (2009), The CALIPSO lidar cloud and aerosol discrimination: Version 2 algorithm and initial assessment of performance. *J. Atmos. Oceanic Technol.*, *26*, 1198–1213, doi:10.1175/2009JTECHA1229.1.

Loeb, N. G., and G. L. Schuster (2008), An observational study of the relationship between cloud, aerosol and meteorology in broken lowlevel cloud conditions, *J. Geophys. Res.*, *113*, D14214, doi:10.1029/2007JD009763.

Moulin, C., C. E. Lambert, F. Dulac, and U. Dayan (1997), Control of atmospheric export of dust from North Africa by the North Atlantic Oscillation, *Nature*, *387*, 691–694, doi:10.1038/42679.

Nalli, N. R., et al. (2005), Profile observations of the Saharan air layer during AEROSE 2004, *Geophys. Res. Lett.*, *32*, L05815, doi:10.1029/2004GL022028.

Nalli, N. R., et al. (2006), Ship-based measurements for infrared sensor validation during Aerosol and Ocean Science Expedition 2004, *J. Geophys. Res.*, *111*, D09S04, doi:10.1029/2005JD006385.

Omar, A. H., et al. (2009), The CALIPSO automated aerosol classification and lidar ratio selection algorithm. *J. Atmos. Oceanic Technol.*, *26*, 1994–2014, doi:10.1175/2009JTECHA1231.1.

Paluch, I. R. (1979), The entrainment mechanism in Colorado cumuli. *J. Atmos. Sci.*, *36*, 2467–2478.

Petters, M. D., and S. M. Kreidenweis (2007), A single parameter representation of hygroscopic growth and cloud condensation nucleus activity, *Atmos. Chem. Phys.*, *7*, 1961–1971, doi:10.5194/acp-7-1961-2007.

Prospero, J. M., and P. J. Lamb (2003), African Droughts and Dust Transport to the Caribbean: Climate Change Implications, *Science*, *302*(5647), 1024–1027.

Prospero, J. M., and T. N. Carlson (1972), Vertical and area distributions of Saharan dust over the western equatorial North Atlantic Ocean, *J. Geophys. Res.*, *77*, 5255–5265.

Prospero, J. M., and R. T. Nees (1977), Dust concentration in the atmosphere of the Equatorial North Atlantic: Possible relationship to the Sahelian drought, *Science*, *196*, 1196–1198.

Reid, J. S., et al. (2002), Dust vertical distribution in the Caribbean during the Puerto Rico Dust Experiment, *Geophys. Res. Lett.*, *29*(7), doi:10.1029/2001GL014092.

Reid, J. S., et al. (2003), Analysis of measurements of Saharan dust by airborne and ground-based remote sensing methods during the Puerto Rico Dust Experiment (PRIDE), *J. Geophys. Res.*, *108*(D19), 8586, doi:10.1029/2002JD002493.

Remer, L. A., et al. (2005), The modis aerosol algorithm, products, and validation, *J. Atmos. Sci.*, *62*, 947–973.

Sassen, K., P. J. DeMott, J. M. Prospero, and M. R. Poellot (2003), Saharan dust storms and indirect aerosol effects on clouds: CRYSTAL-FACE Results, *Geophys. Res. Lett.*, *30*(12), 1633, doi:10.1029/2003GL017371.

Savoie, D. L., J. M. Prospero, and E. S. Saltzman (1989), Non-sea-salt sulfate and nitrate in trade wind aerosols at Barbados: evidence for long-range transport, *J. Geophys. Res.*, *94*(D4), 5069–5080, doi:10.5194/acp-11-557-2011.

Shi, Y., J. Zhang, J. S. Reid, B. Holben, E. J. Hyer, and C. Curtis (2011), An analysis of the collection 5 modis over-ocean aerosol optical depth product for its implication in aerosol assimilation, *Atmos. Chem. Phys.*, *11*, 557–565, doi:10.5194/acp-11-557-2011.

Trapp, J. M., F. J. Millero, and J. M. Prospero (2010), Temporal variability of the elemental composition of African dust measured in trade wind aerosols at Barbados and Miami, *Marine Chemistry*, *120*(1–4), 71–82.

Twohy, C. H., et al. (2009), Saharan dust particles nucleate droplets in eastern Atlantic clouds, *Geophys. Res. Lett.*, *36*, L01807, doi:10.1029/2008GL035846.

Twomey, S. (1959), The nuclei of natural cloud formation. Part II: The supersaturation in natural clouds and the variation of cloud droplet concentration, *Geophys. Pure Appl.*, *43*, 243–249.

Twomey, S. (1977), *Atmospheric aerosols*. Amsterdam: Elsevier Science Publishing Company.

Welton, E., et al. (2000), Ground-based lidar measurements of aerosols during ACE-2: instrument description, results, and comparisons with other ground-based and airborne measurements, *Tellus*, *52B*, 636–651.

Westphal, D. L., O. B. Toon, and T. N. Carlson (1988), A case study of mobilization and transport of Saharan dust, *J. Atmos. Sci.*, *45*, 2145–2175.

Wong, S., and A. E. Dessler (2005), Suppression of deep convection over the tropical North Atlantic by the Saharan air layer, *Geophys. Res. Lett.*, *32*, L09808, doi:10.1029/2004GL022295.

Wong, S., P. R. Colarco, and A. E. Dessler (2006), Principal component analysis of the evolution of the Saharan air layer and dust transport: Comparison between a model simulation and MODIS and AIRS retrievals, *J. Geophys. Res.*, *111*, D20109, doi:10.1029/2006JD007093.

Wu, L. (2007), Impact of Saharan air layer on hurricane peak intensity, *Geophys. Res. Lett.*, *34*, L09802, doi:10.1029/2007GL029564.

Wu, R., B. P. Kirtman, and K. Pegion (2007), Surface latent heat flux and its relationship with sea surface temperature in the National Centers for Environmental Prediction Climate Forecast System simulations and retrospective forecasts, *Geophys. Res. Lett.*, *34*, L17712, doi:10.1029/2007GL030751.

Zhang, J. L., and J. S. Reid (2006), Modis aerosol product analysis for data assimilation: Assessment of over-ocean level 2 aerosol optical thickness retrievals, *J. Geophys. Res. Atmos.*, *111*, D22207, doi:10.1029/2005JD006898.